Chemical Engineering Journal 549 (2026) 183234

Contents lists available at ScienceDirect

Chemical Engineering Journal

journal homepage: www.elsevier.com/locate/cej

On the scaling-up of 3D-printed metallic POCS structured catalysts membrane reactors

I. Gargiulo [a], A. Vita [b], C. Italiano [b], C. Coiana [a,c], F. Gallucci [a,c,*]

[a] Sustainable Process Engineering, Chemical Engineering and Chemistry, Eindhoven University of Technology, the Netherlands
[b] CNR-ITAE "Nicola Giordano", Via Salita S. Lucia Sopra Contesse 5, 98126, Messina, Italy
[c] ZEFIRA BV and 1CUBE BV, Kastanjelaan 400, 5616 LZ, Eindhoven, the Netherlands

ARTICLE INFO

Keywords:
Dip-spin coating scale-up
Periodic Open Cellular Structures (POCS)
Multi-membrane reactor
Ammonia synthesis

ABSTRACT

This work reports the first experimental demonstration of a scaled-up multi-membrane reactor for ammonia synthesis, integrating four tubular carbon molecular sieve membranes (CMSMs) with two 3D-printed metallic Periodic Open Cellular Structure (POCS) supports of Gyroid and Body-Centred Cubic (BCC) geometry, manufactured in Inconel 625 by Laser Powder Bed Fusion and washcoated with a Ru-based catalyst via a scaled-up dip-spin coating procedure. The coating protocol transferred to both topologies at the larger scale without modification, with optical microscopy confirming uniform, crack-free coverage. Novolac-based CMSM carbonized at 550 °C were characterised by organic elemental analysis, XPS, and Raman spectroscopy, confirming a defect-rich, turbostratic sp^2 carbon matrix with microporous architecture. Baseline testing in the conventional reactor over 350–450 °C and 20–40 bar(g) demonstrated that Gyroid and BCC configurations deliver virtually identical catalytic performance, reflecting the dominance of reaction kinetics and thermodynamics over geometry-dependent transport resistances. Upon membrane integration, this geometry-independence was preserved, and the membrane consistently enhanced NH_3 production rates across all operating conditions. Beyond-equilibrium operation, with H_2 conversion and NH_3 yield reproducibly exceeding thermodynamic limits, was achieved exclusively at low wight hourly space velocity (WHSV) and a sweep ratio (SW) of 4: H_2 conversion surpassed equilibrium by 30% at 400 °C and 110% at 450 °C, with NH_3 yield gains of 65% and 170% over the conventional reactor. Scaling from one to four membranes yielded a membrane-area-normalised productivity improvement of up to 424% at 350 °C and 40 bar(g), providing a strong foundation for continued scale-up of membrane reactors for ammonia synthesis.

1. Introduction

Energy-related CO_2 emissions reached an all-time high of 37.8 Gt in 2024, increasing by 0.8% compared to the previous year, with fossil fuels - coal, oil, and natural gas - remaining responsible for the overwhelming majority of anthropogenic greenhouse gas output [1,2]. In 2023, coal alone accounted for 35.5% of electricity production worldwide [3]. An urgent transition to renewables such as hydropower, solar, wind, geothermal, and biomass is thus essential to curb emissions and ensure long-term energy security [4]. Various study have underlined hydrogen as a crucial element in renewable energy systems, given its capacity to provide large-scale energy storage and to mitigate grid imbalance arising from the intermittency of solar and wind generation [5]. Despite its immense potential, hydrogen also faces significant practical challenges: liquefaction demands cryogenic cooling to −253 °C at ambient pressure or compression to ~250 bar at room temperature, yielding an insufficient volumetric energy density of just 2.15 $GJ{\cdot}m^{-3}$. Compounding this, existing infrastructure, such as pipelines, storage tanks, and distribution networks [6], remains insufficient for large-scale deployment [7]. These storage and transportation barriers have prompted researchers to explore indirect hydrogen carriers, with chemical compounds such as alcohols, ammonia, and hydrocarbons emerging as promising solutions [8]. Ammonia, in particular, liquefies under mild conditions, either by cooling to −33.3 °C at atmospheric pressure or by compression to approximately 8.6 bar at 20 °C. It also offers a higher volumetric energy density than liquid hydrogen, and exhibits low flammability (high flash point), rendering it far safer to handle and transport. When produced from renewable hydrogen via electrolysis, so-called green ammonia [9], it offers a carbon-neutral

* Corresponding author at: Sustainable Process Engineering, Chemical Engineering and Chemistry, Eindhoven University of Technology, the Netherlands.
E-mail address: f.gallucci@tue.nl (F. Gallucci).

https://doi.org/10.1016/j.cej.2026.183234
Received 9 August 2026; Received in revised form 9 October 2026; Accepted 17 October 2026
Available online 18 October 2026
1385-8947/© 2026 The Authors. Published by Elsevier B.V. This is an open access article under the CC BY license (http://creativecommons.org/licenses/by/4.0/).

Nomenclature

Symbol

A_{mem}	Total active membrane area, m^2
F_i^R	Molar flow rate of species i in the retentate, mol s^{-1}
F_i^P	Molar flow rate of species i in the permeate, mol s^{-1}
$F_{i,in}^R$, $F_{i,out}^R$	Molar flow rate of species i at the inlet /outlet of the retentate, mol s^{-1}
$F_{i,in}^P$, $F_{i,out}^P$	Molar flow rate of species i at the inlet /outlet of the peremate, mol s^{-1}
$F_{i,tm}$	Net trans-membrane molar flow of species i from retentate to permeate, mol s^{-1}
$F_{i,tm}^*$	Trans-membrane molar flow from permeate to retentate (co-feeding), mol s^{-1}
$F_{NH_3}^{tot}$	Total NH_3 molar flow produced (retentate + permeate), mol s^{-1}
P	Pressure, bar
ΔP	Transmembrane pressure difference, bar
SW	Sweep-gas-to-feed molar ratio, –
T	Temperature, °C
WHSV	Weight hourly space velocity, mLn g_{cat}^{-1} h^{-1}
w_{cat}	Catalyst mass, g
x_{H_2}	H_2 conversion, %
Y_{NH_3}	NH_3 yield, %

Superscripts

R	Retentate (reaction) side
P	Permeate side
SCR	Structured catalyst reactor (conventional)
SCMR	Structured catalyst membrane reactor

Subscripts

i	Species (H_2, N_2, NH_3)
in, out	Inlet, outlet
tm	Trans-membrane

energy vector and fertilizer feedstock, directly decoupling food and energy security from fossil fuel dependence. With global ammonia production reaching approximately 185 million tonnes per year and contributing roughly 2.4 kg CO_2 per kg NH_3 [10], a transition to green ammonia synthesis could eliminate over 440 million tonnes of CO_2 annually, making it one of the most impactful decarbonization levers available.

Ammonia is industrially synthesized by reacting nitrogen and hydrogen via the reversible, exothermic Haber-Bosch reaction:

$$N_2 + 3H_2 \rightleftharpoons 2NH_3 \Delta H_{298K} = -92\ kJ\ mol^{-1}$$

Since the reaction is exothermic and proceeds with a reduction in the number of moles, it is thermodynamically favoured at low temperature and high pressure, but kinetically very slow unless relatively high temperatures and a suitable catalyst are employed [11]. Owing to continuous process and catalyst development, modern plants typically operate at pressures of about 80–120 bar, significantly lower than the 150–300 bar range of early Haber-Bosch units, while maintaining competitive performance [12]. Nevertheless, the single-pass conversion remains relatively low (on the order of 10–20%), necessitating a large recycle loop to achieve overall conversions above 95% and contributing to the high energy intensity of conventional ammonia production [13], which accounts for approximately 1–2% of global energy consumption. Non-thermal plasma can produce ammonia at milder bulk conditions by activating nitrogen in the plasma phase, but current systems are highly energy-intensive and inefficient, limiting them to small-scale or niche applications [14]. Electrochemical ammonia synthesis likewise enables direct electricity-to-ammonia conversion, yet it suffers from low ammonia formation rates, competing hydrogen evolution, materials degradation, and poor overall efficiency, so it cannot presently compete with large-scale Haber-Bosch plants.

Achieving a step-change reduction in the energy and carbon intensity of ammonia synthesis requires moving beyond incremental optimisation of the Haber-Bosch cycle toward fundamentally intensified process configurations that simultaneously address both thermodynamic and transport limitations [15]. Catalytic membrane reactors have recently been proposed as a particularly promising intensified configuration, overcoming the thermodynamic constraints of the Haber-Bosch process by coupling reaction with selective in-situ ammonia removal in a single unit [16]. By continuously removing NH_3 from the reaction zone, the membrane displaces the reaction equilibrium beyond its thermodynamic limit, enabling equivalent or higher conversions at significantly reduced temperatures and pressures compared to the conventional process.

Several membrane concepts have been investigated for ammonia separation under relevant catalytic conditions. Functionalized polymer and organosilica membranes (e.g. Poly(vinylammonium Thiocyanate) [17], Nafion [18], Aquivion [19]) offer a favourable compromise between NH_3 permeability and selectivity and are relatively straightforward to fabricate and scale. However, most of them decompose below 200 °C, making them unsuitable for the ammonia synthesis application. Alternative inorganic or solvent-based systems exhibit very high intrinsic selectivities but are often limited by low permeance, stability issues, or challenges in scale-up, which restrict their suitability for large-scale ammonia production [20]. For instance, Na^+-gated nanochannel membranes display exceptional NH_3/H_2 and NH_3/N_2 selectivities (up to 10^3 - 10^4) obtained at 150 °C and 21 bar, with selectivities as high as 300 maintained up to 250 °C and 35 bar, but at only moderate NH_3 permeance [21,22]. Sulfonated organosilica (TPS) membranes can operate at approximately 300 °C with NH_3 permeance on the order of 10^{-7} mol m^{-2} s^{-1} Pa^{-1} and NH_3/H_2 and NH_3/N_2 selectivities of about 7 and 266, respectively, yet their flux-selectivity balance still falls short of industrial requirements [23,24]. $ZnCl_2$-immobilized molten-salt (IMS) membranes exhibit outstanding NH_3 separation performance at 300–350 °C, with NH_3/N_2 and NH_3/H_2 selectivities exceeding 1000 and 3000, but their long-term stability and durability under cyclic high-temperature operation remain uncertain [25]. Carbon molecular sieve (CMS) membranes represent a particularly promising alternative in this landscape. Derived from the pyrolysis of polymeric precursors, CMSMs combine the molecular sieving capability of inorganic membranes with a degree of tunability in pore size distribution, and have demonstrated thermal stability well above 300 °C [26]. Their separation mechanism relies also on the selective adsorption and surface diffusion of NH_3 through micropores, exploiting the difference in kinetic diameter and polarity between NH_3, H_2, and N_2. Unlike polymeric membranes, CMSMs do not suffer from decomposition at elevated temperatures [27], and can be fabricated in tubular geometries directly compatible with multi-membrane reactor configurations, making them uniquely suited for integration with structured catalyst supports under conditions relevant to ammonia synthesis. Notably, our group has previously demonstrated [28] that a tubular CMSM integrated with a Ru-based Gyroid Periodic Open Cellular Structure (POCS) catalyst outperforms the equivalent conventional reactor across the full range of operating conditions investigated, confirming the viability of this membrane class for equilibrium-shift ammonia synthesis at the laboratory scale. That earlier work, however, was limited to technology readiness level (TRL) 3–4, using small Gyroid pieces and a single membrane, leaving open the questions of scalability, multi-membrane integration, and geometry

dependence that the present work addresses.

While membrane reactors offer a compelling route to overcome the thermodynamic constraints of ammonia synthesis, their practical performance is equally governed by the catalytic architecture housed within the reactor. In conventional packed-bed configurations, pellet beds introduce significant pressure drop [29], poor radial heat distribution, and channelling effects [30] that become increasingly detrimental at the modest pressures and temperatures favoured by membrane reactor operation. Realising the full potential of membrane-assisted equilibrium shift therefore requires not only a selective and permeable membrane, but also a catalyst support that enables uniform flow distribution, efficient heat and mass transfer, and low pressure drop - properties that conventional pellet beds struggle to deliver simultaneously. This has motivated growing interest in structured catalyst supports as an enabling technology for next-generation intensified reactors, where the geometry of the support itself becomes a design variable alongside operating conditions and membrane properties. Structured catalysts consist of ceramic or metallic substrates, pre-shaped in the form of a single continuous structure with stable geometry over which the catalytically active sites are properly dispersed [31]. The development of highly efficient structured catalysts is attracting increasing attention for process intensification in catalytic reactors, particularly in applications involving heat and mass transfer limitations such as ammonia synthesis and decomposition, methanation, and hydrogen production processes [32].

In this context, three-dimensional (3D)-printed metallic Periodic Open Cellular Structures (POCS) have attracted growing interest as catalyst supports able to overcome the well-known limitations of pellet-packed beds in terms of pressure drop, intra-bed temperature gradients, and uniformity of fluid distribution [33]. Among the proposed lattices, the Triply Periodic Minimal Surface (TPMS) Gyroid offers curvature-driven mixing along smooth, fully interconnected channels and a high surface-area-to-volume ratio [34,35], while the Body-Centred Cubic (BCC) geometry provides a more open channel network with comparatively lower pressure drop [36].

To the best of our knowledge, no study has yet reported the integration of 3D-printed metallic POCS catalysts with carbon molecular sieve membranes for ammonia synthesis at a scale beyond TRL 3–4, nor a systematic comparison of POCS lattice geometries has been reported within an operational ammonia synthesis membrane reactor. This work therefore represents the first demonstration of dual process intensification, combining structured catalytic supports with membrane-assisted equilibrium shift, at a scale and configuration relevant to pilot-scale deployment (TRL 5). Two complementary 3D-printed metallic POCS architectures, Gyroid and BCC, were manufactured in nickel alloy (IN625) with dimensions 5.1 × 10 cm (~130 cm^3 per piece). Both geometries were then activated with the same Ru-based catalyst through a scaled-up dip-spin coating procedure, designed to meet the higher slurry demand, and integrated with four tubular CMSMs in a multi-membrane reactor.

The objectives of the study are: (i) to demonstrate that the dip-spin coating protocol previously optimised at the lab scale can be reproducibly transferred to larger supports of different lattice topology, without modification of the slurry formulation, the spinning parameters, or the number of coating cycles; (ii) to provide a direct comparison of the Gyroid and BCC geometries when integrated with CMSMs in the membrane reactor; (iii) to quantify the enhancement in NH_3 production rate, H_2 conversion and NH_3 yield attributable to membrane-assisted equilibrium shift, including the influence of increased membrane area, and to identify the operating conditions under which this synergy between structured catalytic supports and CMS membranes is maximised.

2. Experimental

2.1. Materials and preparation

2.1.1. POCS design and fabrication: Gyroid and BCC geometry

Periodic Open Cellular Structures (POCS) with Gyroid and Body-Centred Cubic (BCC) geometries were manufactured by ENGIE in Inconel 625 (IN625) by Laser Powder Bed Fusion (LPBF) starting from CAD-designed architectures. Cylindrical supports with an external diameter of 51.1 mm and a length of 100 mm were produced. For each geometry, two identical pieces were stacked axially in series within the reactor, yielding a total catalytic bed length of 200 mm per geometry. Two Gyroid and two BCC structures were fabricated to accommodate a total of four tubular carbon molecular sieve membranes (CMSMs) within the multitubular membrane reactor configuration. Each structure incorporated four longitudinal channels (Ø = 15.1 mm) aligned along the axial direction; when the two pieces of the same geometry are assembled in series, these channels form continuous conduits of 200 mm that house the CMSMs (220 mm in active length), which extend slightly beyond the POCS assembly to span the full reactor housing.

The Gyroid architecture was characterised by a cell size of 5 mm and a sheet thickness of 0.34 mm, whereas the BCC structure exhibited a cell size of 3 mm and a strut diameter of 0.40 mm. Both geometries present high void fractions ($\varepsilon \approx 0.72–0.82$). Fig. 1 shows a rendering of the single-unit cells corresponding to both Gyroid and BCC supports, together with optical microscope images of representative portions of their bare surfaces. Dimensional measurements revealed good agreement between the CAD-designed geometries and the resulting additively manufactured structures, confirming the fidelity and reproducibility of the printing process.

Prior to catalyst deposition, each as-built support was degreased under ultrasonic agitation in a 50:50 vol% acetone/water mixture for 30 min, rinsed with abundant distilled water, and oven-dried at 120 °C for 1 h. A pre-oxidation treatment in static air at 900 °C for 6 h was then applied to all supports to develop a thin, adherent oxide scale on the metallic surface, thereby improving the adhesion of the subsequent washcoat layer [37].

2.1.2. Catalyst slurry preparation

A developmental Ru-based catalyst (2.2 wt% Ru) supplied by Johnson Matthey in powder form was used to prepare the washcoat slurry employed for activating the four POCS supports. The target catalyst loading was set at 0.21 g cm^{-3}.

Four slurry batches (I-IV) were prepared to meet the catalyst demand associated with the larger support volume of about 130 cm^3 each, corresponding to the structure envelope excluding the four membrane channels, each with a volume of approximately 150 mL. The slurry composition was kept unchanged with respect to the formulation reported in our previous work [28]: 35 g (22.4 wt%) catalyst, 66.5 g (42.5 wt%) glycerol, 2.38 g (1.5 wt%) polyvinyl alcohol (PVA) and 33.6 wt% distilled water. The dispersion medium was prepared by dissolving PVA (87–89% hydrolysed, Sigma-Aldrich) in distilled water, under magnetic stirring at 85 °C, followed by the addition of glycerol (99.5% bi-distilled, Analar Normapur®). In this formulation, glycerol acts as a dispersant, PVA as a rheology modifier, and distilled water as solvent and diluent. Prior to incorporation into the slurry, the catalyst powder was pre-milled in zirconia jars for 3 h at 300 rpm to reduce particle size and improve dispersion. The catalyst powder was then added to the dispersion medium, and the resulting slurry was homogenised by ball milling (BM40-POWTEQ) with zirconia spheres (1 cm diameter, sphere-to-powder mass ratio = 7:1) for 24 h at 300 rpm. To increase throughput at this scale, four 250 cm^3 zirconia jars were loaded and operated simultaneously in the planetary mill, allowing batches I-IV to be processed in a single milling run. After milling, each batch underwent a 30 min sonication treatment to minimise foaming prior to coating.

The rheological behaviour of all four slurry batches was

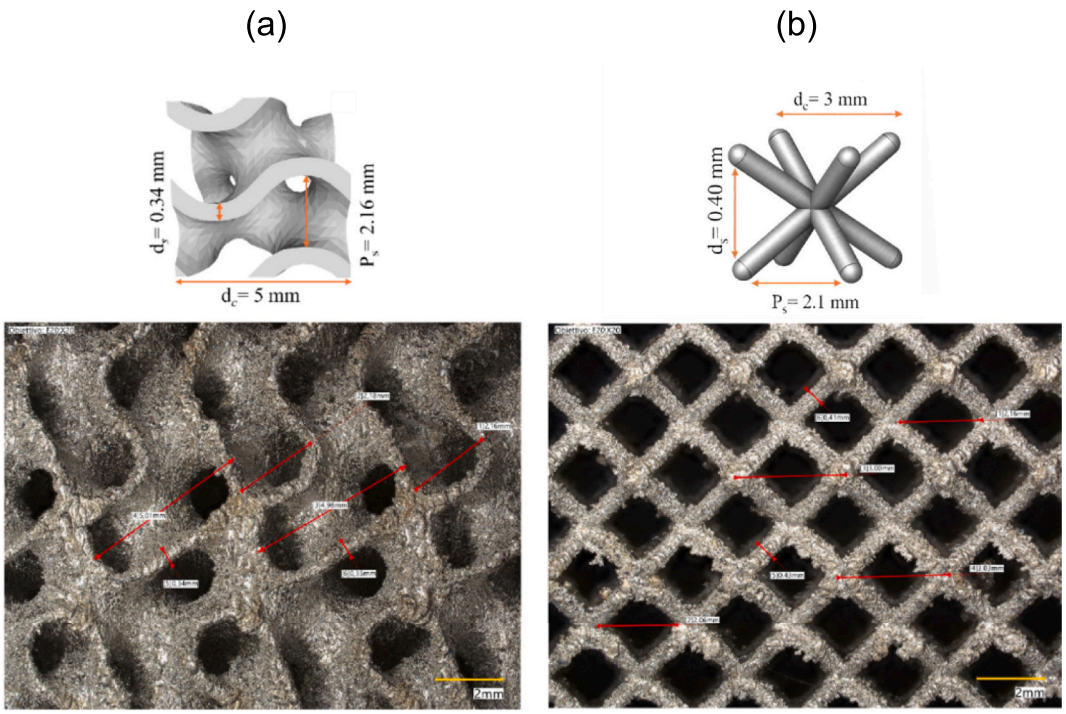

Fig. 1. Unit cells rendering and optical images of Gyroid (a) and BCC (b); d_c represents the cell dimension, d_s the thickness of the sheet and P_s the equivalent pore size dimension.

characterised over the shear-rate range 0.1–2000 s^{-1}; the results are reported and discussed in Section 3.1. All four batches exhibited equivalent pseudoplastic, shear-thinning behaviour across the full shear-rate window investigated, confirming excellent batch-to-batch reproducibility of the scaled-up preparation procedure.

2.1.3. POCS activation by dip-spin coating

The activation of the four POCS supports - two Gyroid and two BCC - was carried out by a combined dip-spin coating route, developed and optimised in our previous work on smaller Gyroid geometries [38]. In each coating cycle, the support was fully immersed in the slurry for approximately 10 s to ensure complete wetting of the open-cell network. The wet sample was immediately transferred to a commercial spin-coater (Laurell WS-650Mz-23 NPPB), where the excess slurry was removed by rotating the piece at 1000 rpm for 20 s, with a ramp acceleration of 1000 rpm s^{-2}. To accommodate the larger POCS dimensions, a dedicated cylindrical specimen holder was designed and integrated into the spin-coating system, ensuring mechanical stability and alignment during high-speed rotation. Immediately after spinning, the support was flash-dried in air at 450 °C for 10 min to consolidate the freshly deposited layer before the next dipping step.

The dip-spin-flash-dry sequence was iterated 16 times per support until the gravimetric uptake matched the target loading of 0.21 g cm^{-3} (≈ 27 g of washcoat per piece). The progression of the coating was monitored gravimetrically throughout: each sample was weighed before and after every drying and calcination step, so that the build-up of the washcoat could be tracked cycle-by-cycle and the nominal loading verified at the end of the process.

Once the target loading was achieved, all four supports underwent a final calcination in static air at 500 °C for 6 h (heating rate 5 °C min^{-1}) to remove residual organic additives (PVA and glycerol) and stabilise the catalyst layer. The Gyroid and BCC supports obtained at the end of the activation procedure are shown in Fig. 2.

2.1.4. Membrane fabrication

A Novolac-based precursor for the carbon molecular sieve (CMS) membranes was prepared according to the method described in [28], using the same phenol-formaldehyde monomer ratio, acid catalyst, Cu addition, and thermal treatment conditions up to the polymerisation stage. This synthesis route was employed by TECNALIA to obtain both supported CMS membranes for catalyst-integrated reactor experiments and unsupported membrane material for ex situ characterization.

For the supported membranes, the precursor solution was deposited onto asymmetric porous α-Al_2O_3 tubes ($Ø^{in}$ = 7 mm, $Ø^{ex}$ = 10 mm, outer surface pore size ~100 nm), geometry, surface preparation, and coating conditions as described in [28]. After deposition, the coated tubes were

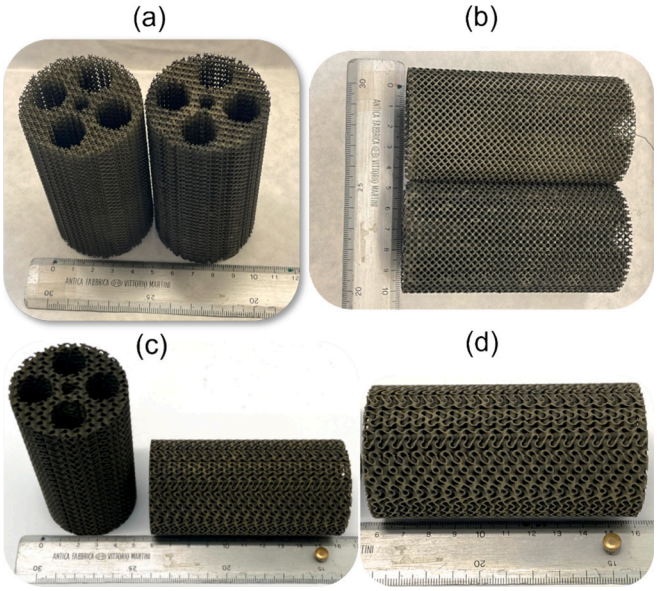

Fig. 2. Images of 3D-printed washcoated structured catalysts: (a)-(b) Gyroid topology and (c)-(d) Body-Centred Cubic (BCC) topology supports after coating deposition.

subjected to the same polymerisation and subsequent carbonization protocol, carried out under a non-oxidising atmosphere at 550 °C. Unsupported membrane samples were prepared in parallel from the same Novolac-based precursor, in the absence of any ceramic substrate. Two sample states were produced: a non-carbonized sample, obtained by polymerisation at 90 °C without any subsequent thermal treatment, and a carbonized sample, produced by applying the same carbonization protocol as the supported membranes.

2.2. Characterizations technique

2.2.1. Morphological and rheological characterization

The surface morphology and geometric fidelity of the as-built and washcoated Gyroid and BCC supports were assessed by optical microscopy using a Keyence VHX-7000 digital microscope. Images were acquired with VHX-E20 (High-Resolution, Low-Magnification Objective Lens 20–100×) and VHX-E100 (High-Resolution, Medium-Magnification Objective Lens 100–500×) objective lenses at multiple locations across the strut and sheet surfaces and cell interiors. Cell size, strut diameter, sheet thickness, and channel diameter were measured and compared against the nominal CAD dimensions to quantify the dimensional deviations introduced by the LPBF process.

The rheological behaviour of the washcoat slurry was characterised using a modular compact rotational rheometer (Modular Compact Rheometer MCR 92, Anton Paar GmbH, Graz, Austria) equipped with a double-gap measuring geometry. Flow curves were acquired at 25 °C over a shear-rate range of 0.1–3000 s^{-1}.

2.2.2. Unsupported carbon membrane material characterization

The unsupported CMS membrane material was characterised in both the non-carbonized and carbonized (550 °C) states by organic elemental analysis (OEA), X-ray photoelectron spectroscopy (XPS), and Raman spectroscopy, to track the chemical and structural transformation induced by pyrolysis.

Elemental composition (C, H, N, O) was determined by OEA using a Thermo Scientific Flash Smart CHNS/O analyzer (Waltham, MA, USA).

XPS measurements were performed under ultra-high vacuum using a K-Alpha spectrometer (Thermo Scientific™). Spectral processing was carried out in CasaXPS software, applying a Shirley-type background subtraction prior to peak fitting. Component fitting was performed following the methodology reported in [39].

Raman spectroscopy was carried out using a WITec WMT 50 confocal Raman microscope equipped with a 532 nm excitation laser under confocal conditions, providing high spatial resolution. Spectra were collected for both the non-carbonized precursor and the carbonized membrane (550 °C) to assess the changes in carbon ordering and bonding structure induced by thermal treatment, and were baseline-corrected prior to analysis to remove background fluorescence and isolate the intrinsic Raman signal.

2.2.3. Experimental setup

The experimental test rig used for testing has been described in detail in the previous work [28], to which the reader is referred for a comprehensive account of the gas supply system, flow control instrumentation, thermal management, pressure regulation, and analytical equipment. Briefly, the setup comprises Bronkhorst mass-flow controllers for N_2, H_2, and NH_3, pneumatically actuated Swagelok valves, independent back-pressure regulators on the retentate and permeate sides, and a Compact GC 4.0 micro-gas chromatograph (Global Analyzer Solutions) for multi-component gas analysis, with methane as internal standard. The P&ID of the complete setup is shown in Fig. 3, illustrating the gas feed lines, MFC network, reactor section, back-pressure regulators, and downstream GC analysis system.

The present study introduces a scaled-up multi-membrane reactor configuration, designed to accommodate four tubular CMSMs integrated with the POCS catalyst unit. The reactor consists of a 316Ti stainless steel pressure vessel ($Ø^{ex} = 60$ mm, $Ø^{in} = 51.3$ mm, L = 350 mm), sealed at the top flange via a LEADER Ring Joint R Oval sealing ring (316 L,

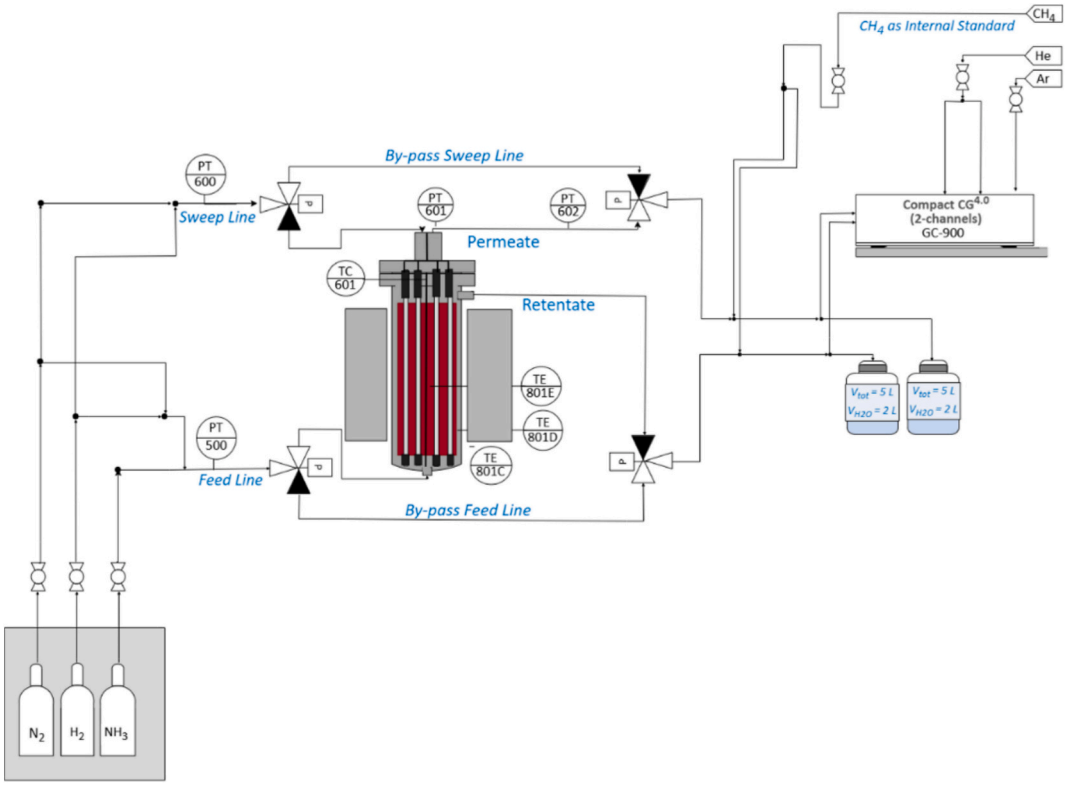

Fig. 3. P&ID of the experimental setup.

R24, API 6A/ISO 10423), selected for its mechanical and chemical compatibility with high-pressure ammonia service. The four membranes are individually sealed to the top flange via Swagelok connections incorporating graphite rings to mitigate mechanical stress on the membrane tubes, resulting in an overall active membrane length of approximately 220–225 mm. Two POCS segments are stacked axially in series within the vessel, yielding a total active bed length of 200 mm. A multipoint thermocouple is embedded within the POCS bed along its central axis to monitor the axial temperature profile across the full catalytic zone and to detect any thermal gradients arising during reaction. A 3D render of the multi-membrane reactor design, together with the as-built demonstrator unit and the metallic sealing components, is shown in Fig. 4.

To ensure co-current operation, the reaction stream enters from the bottom of the reactor, while the sweep gas is introduced from the top via four individual internal capillaries ($Ø^{ex}$ = 3.3 mm), each inserted into one of the four CMSMs, extending to the end of the respective membrane and then flowing back along its length in the same axial direction as the retentate stream. The permeate stream is collected at the top flange and withdrawn independently from the retentate. Fig. 5(a) shows the four CMSMs extending from the top flange with their individual Swagelok fittings, while Fig. 5(b) illustrates the subsequent assembly step in which the POCS catalyst unit has been positioned over the membranes prior to insertion into the pressure vessel.

2.2.4. Operating conditions and key performance indicator (KPI)

Two reactor configurations were tested: the structured catalyst reactor (SCR), i.e. the conventional reactor in which the POCS catalyst was tested without membrane integration, (with the membrane channels replaced by dense tubes/closed), and the structured catalyst membrane reactor (SCMR), in which the POCS catalyst was integrated with the CMSMs for in-situ NH_3 removal. The operating conditions explored in this study are summarised in Table 1. The weight hourly space velocity (WHSV) is defined as the total volumetric flow rate of the reactant feed (H_2 + N_2) at normal conditions divided by the catalyst mass. In all experiments, the reactor was fed with an H_2:N_2 molar ratio of 2:1. In the membrane reactor (SCMR) tests, the sweep gas had the same composition as the reactor feed (H_2:N_2 = 2:1), in order to keep similar H_2 and N_2 partial pressures on both sides of the membrane and limit reactant losses from the reaction zone. The sweep ratio (SW) is defined as the ratio between the molar flow rate of the sweep gas fed to the permeate side and the molar flow rate of the feed to the retentate side. Unless otherwise stated, the permeate side was operated at the same pressure as the retentate side. The effect of a transmembrane pressure difference (ΔP = 1, 2 and 3 bar) was investigated only at WHSV = 3285 mLn g_{cat}^{-1} h^{-1} and SW = 1, as discussed in Section 3.7.

For each experimental condition, the reactor performance was evaluated through a set of metrics defined below, designed to account for the non-ideal behaviour of the membrane which results in partial permeation of unreacted H_2 and N_2.

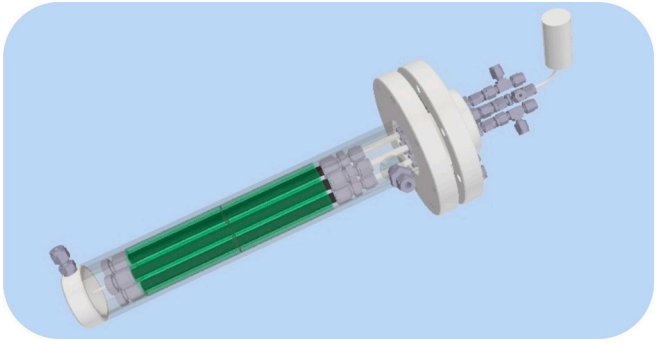

Fig. 4. 3D CAD render of the multi-membrane reactor showing the four tubular CMSMs running axially through the POCS catalyst body (green) housed within the cylindrical pressure vessel, with the top flange and Swagelok membrane fittings.

Fig. 5. (a) Assembly of four tubular CMS membranes connected to the reactor flange, (b) with POCS catalyst structures fitted over the membrane tubes.

Table 1
Operating conditions used during the experimental campaign.

Case ID	WHSV [mLn g_{cat}^{-1} h^{-1}]	T [°C]	P [bar]	ΔP [bar]	SW [−]	H_2:N_2
SCR	715	350, 400, 450	20, 30, 40	–	–	2
SCR	3285	350, 400, 450	30, 40	–	–	2
SCMR	715	350, 400, 450	30, 40	0	1	2
SCMR	715	350, 400, 450	20, 30, 40	0	4	2
SCMR	3285	350, 400, 450	30, 40	0, 1, 2, 3	1	2

$$\%x_{H_2} = \frac{F^R_{H_2,in} - F^R_{H_2,out} - F_{H_2,tm}}{F^R_{H_2,in} - F_{H_2,tm}^{*}} \times 100 \quad (1)$$

$$F_{H_2,tm} = F^P_{H_2,out} - F^P_{H_2,in} \quad (2)$$

$$F_{H_2,tm}^{*} = F^P_{H_2,out} - F^P_{H_2,in} \text{ only if } F_{H_2,tm} \leq 0 \text{ cofeeding} \quad (3)$$

$$\%Reactant\ loss = \frac{F_{i,tm}}{F^R_{i,in}} \times 100 \quad (4)$$

$$\%Recovery\ factor = \frac{F^P_{NH_3}}{F^R_{NH_3} + F^P_{NH_3}} \times 100 \quad (5)$$

$$\%Y_{NH_3} = \frac{F^R_{NH_3} + F^P_{NH_3}}{F^R_{H_2,in} - F_{H_2,tm}^{*}} \quad (6)$$

$$NH_3\ production\ rate - catalyst - based = \frac{F^R_{NH_3} + F^P_{NH_3}}{w_{cat}} \quad (7)$$

$$NH_3\ production\ rate - membrane - based = \frac{F^R_{NH_3} + F^P_{NH_3}}{A_{mem}} \quad (8)$$

$$\%Improvement = \frac{KPI_i^{SCMR} - KPI_i^{SCR}}{KPI_i^{SCR}} \times 100 \quad (9)$$

$$\%Improvement\ of\ membrane\ area\ normalised\ NH_3\ productivity = \frac{F^{tot}_{NH_3,4\ mem.} - F^{tot}_{NH_3,1\ mem.}}{F^{tot}_{NH_3,1\ mem.}} \times 100 \quad (10)$$

The H_2 conversion definition (Eq. (1)) corrects the conventional conversion expression to account for the fact that a fraction of the H_2 fed to the retentate may permeate through the membrane without participating in the reaction. When $F_{H_2,tm} > 0$, (Eq. (2)) H_2 is lost from the retentate to the permeate (a reactant loss scenario) and this lost H_2 must be excluded from both the numerator and denominator of the conversion expression. When $F_{H_2,tm} < 0$, (Eq. (3)) the flux direction reverses, indicating that H_2 present in the sweep stream enters the retentate through the membrane (a co-feeding scenario). The fractional loss of reactant species *i* (H_2 or N_2) to the permeate side is quantified according to Eq. (4). The NH_3 recovery factor (Eq. (5)) represents the fraction of the total ammonia produced that is collected on the permeate side: a high recovery factor reflects efficient NH_3 extraction from the reaction zone. The NH_3 yield (Eq. (6)) is defined on the basis of the total NH_3 produced across both retentate and permeate streams, normalised by the effective H_2 feed available for reaction. The denominator accounts for the co-feeding correction when applicable, ensuring that the yield reflects only the H_2 that is genuinely available for synthesis. The NH_3 production rate is reported in two complementary forms. The catalyst-normalised rate (Eq. (7)) enables direct comparison of catalytic activity across different geometries, whereas the membrane-area-normalised productivity (Eq. (8)) provides a complementary figure that quantifies the NH_3 output per unit of membrane surface area deployed, particularly important during the scaling of membrane reactor. All catalyst-normalised NH_3 production rate data are reported with error bars representing the standard deviation computed from five consecutive gas chromatography measurements acquired under steady-state conditions at each operating point. The relative performance improvement of the membrane reactor over the conventional reactor is defined as Eq. (9) at identical operating condition, whereas the incremental gain attributable to increasing the number of integrated membranes from one to four is quantified by the membrane-area-normalised productivity improvement in Eq. (10), using the NH_3 membrane area based production rate (Eq. (8)).

These metrics are used in Section 3 to assess the performance of the four-membrane reactor configuration and to compare it against the single membrane baseline reported in our previous work. It should be noted that the two configurations differ in both membrane number and catalyst mass, with the catalyst loading and membrane area scaled approximately in proportion.

3. Results and discussion

3.1. POCS catalyst: slurry rheology and batch reproducibility

The rheological behaviour of the four slurry batches was investigated over the shear-rate range 0.1–2000 s^{-1}; the resulting dynamic viscosity curves are reported in Fig. 6. All four batches exhibit a consistent pseudoplastic, shear-thinning response. At very low shear rates (~0.1–0.2 s^{-1}), the viscosity passes through a local maximum of approximately 0.08–0.10 Pa·s, attributed to the progressive breakdown of the weakly structured polymer-solvent network formed at rest. With increasing shear rate, the viscosity decreases monotonically by nearly one order of magnitude, approaching a Newtonian-like plateau of ~0.02 Pa·s above ~100 s^{-1}.

This flow profile is well matched to the dip-spin coating procedure adopted in this work. The comparatively higher viscosity at low shear promotes sufficient slurry retention on the POCS struts during the dipping step, while the low plateau viscosity at high shear, representative of the spinning stage, allows excess slurry to drain freely, preventing channel blockage within the open-cell architecture and promoting a uniform catalyst distribution across the lattice. Most importantly, the curves measured for batches I-IV are superimposable across the entire shear-rate window investigated, confirming the excellent batch-to-batch reproducibility achieved by operating four 250 cm^3 zirconia jars simultaneously in the planetary mill.

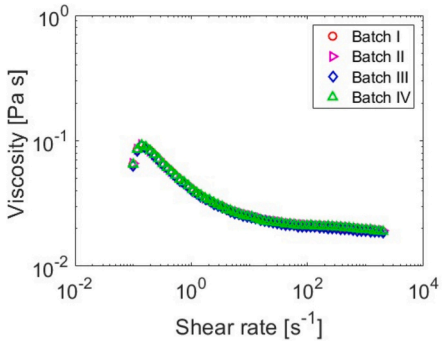

Fig. 6. Slurry rheological behaviour.

3.2. Optical characterization of the activated POCS supports

Representative optical images of the external surface of the activated POCS supports, acquired with a digital optical microscope (Keyence VHX-7000), are reported in Fig. 7**:** the left panel refers to the Gyroid geometry and the right panel to the BCC. In both cases, the catalyst layer appears uniformly distributed over the metallic struts, with full surface coverage and no evidence of cracking, delamination, or localised slurry accumulation within the channels. The native architecture of each support, the smoothly curving cells of the Gyroid and the more angular periodically arranged windows of the BCC, is fully preserved after activation, and all open-cell pathways remain clearly accessible to gas flow.

These observations confirm the effectiveness of the dip-spin coating procedure in producing a thin, conformal washcoat on both POCS architectures. The spin-coating step proved particularly critical in this regard: rotating the wet support at 1000 rpm efficiently removed excess slurry retained within the lattice, yielding a coating layer thick enough to meet the target loading yet thin enough to avoid pore occlusion, which would otherwise penalise flow distribution and active-site accessibility.

Notably, an identical protocol - i.e. slurry formulation, dipping time, spinning rate and acceleration, number of dip-spin cycles, and flash-drying conditions - was applied without modification to both POCS geometries, despite their markedly different topological character, and yielded coating quality of comparable standard across both architectures. This geometry-independence demonstrates that the proposed dip-spin coating route is robust with respect to support topology and scale,

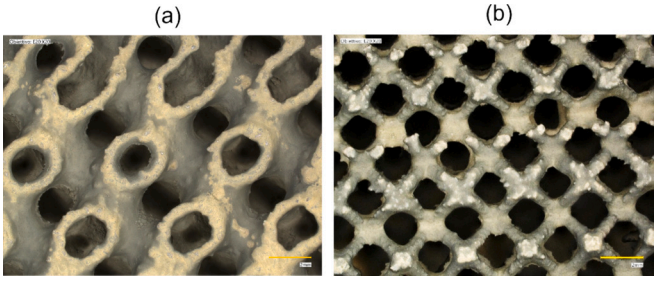

Fig. 7. Optical images of the washcoated surface of structured catalyst supports: (a) Gyroid topology and (b) Body-Centred Cubic (BCC) topology.

and constitutes a viable and readily transferable strategy for the catalytic activation of complex metallic 3D-printed structures.

3.3. Membrane material characterization

The chemical composition of the Novolac-based membrane material was investigated before and after carbonization at 550 °C by organic elemental analysis (OEA), X-ray photoelectron spectroscopy (XPS), and Raman spectroscopy. The three techniques provide complementary and mutually consistent evidence of the polymer-to-carbon transformation, and their findings are discussed jointly below.

OEA reveals a marked compositional shift upon carbonization, as summarised in Table 2. The pre-carbonized sample exhibits a carbon content of 73.9 wt%, with substantial contributions from hydrogen (6.7 wt%), oxygen (14.7 wt%), and nitrogen (4.7 wt%), consistent with the composition expected for a Novolac resin incorporating an ethylenediamine crosslinker and residual NMP solvent. After carbonization, the carbon content rises to 92.0 wt%, while hydrogen, oxygen, and nitrogen decrease sharply to 3.3, 3.8, and 0.9 wt%, respectively. The near-complete elimination of hydrogen is indicative of extensive dehydrogenation and condensation reactions during pyrolysis, while the reduction in oxygen and nitrogen reflects the thermal decomposition of phenolic hydroxyl groups, methylene ether bridges, and amine-based functionalities. The residual heteroatom content in the carbonized sample suggests that a fraction of surface oxygen and nitrogen groups survives pyrolysis. The OEA findings are corroborated by the elemental composition of the samples determined through XPS analysis (Table 2). The XPS C1s spectra provide surface-specific confirmation of the bulk compositional changes observed by the elemental analysis. In the pre-carbonized sample Fig. 8(a), the C1s envelope is broad and asymmetric, comprising a dominant C—C component at ~284.8 eV together with C—O contribution at ~286.2 eV attributed to aliphatic esters, phenolic hydroxyl groups, and methylene ether bridges of the Novolac backbone. The C═O component at ~288.2 eV reflects carbonyl-type species, mainly the lactam carbonyl of NMP along with possible oxidized carbonyl groups formed within the phenolic backbone [39–41]. A weak shake-up satellite at ~290.5 eV, arising from $\pi \rightarrow \pi^*$ transitions in which the photoionised system is left in an electronically excited state a few electron volts above the ground state [42], confirms the presence of aromatic rings within the Novolac structure. After carbonization Fig. 8(d), the C1s envelope undergoes a marked transformation: the C—C component becomes dominant, reflecting the conversion of the sp^3-rich polymer matrix to a predominantly sp^2 graphitic-like carbon network, while the C—O contribution is now positioned at ~285.6 eV and shows reduced intensity, in full agreement with the oxygen elimination observed by elemental analysis. Additionally, the C═O component is replaced by a very weak COO contribution at ~288.6 eV, indicating the evaporation of NMP and the emergence of carboxyl/ester groups formed through thermally induced rearrangements during pyrolysis [43]. The O1s spectra are coherent with the C1s curve fitting and furtherly support the compositional changes. In the pre-carbonized sample Fig. 8(b) the spectrum comprises the C—O contribution at ~532.9 eV associated with phenolic O—H groups and possible methylene-ether bridges, and the C═O component at ~531.5 eV corresponding to amide/lactam carbonyls from NMP together with oxidized carbonyl species formed within the Novolac matrix [44,45]. After carbonization Fig. 8(e), the total oxygen signal decreases substantially, consistent with the reduction from 14.7 to 3.8 wt% measured by OEA and from 22.3 wt% to 5.5 wt% determined by XPS. The shape of the O1s spectrum changes markedly, displaying a double-peaked structure whose curve fitting resolves four distinct contributions. These include oxidized copper species (Cu_xO) at ~531 eV, a C-OH/C-O-C/C-OR component at ~532.2 eV, a COOR contribution at ~533.7 eV, and a high binding energy feature at ~534.7 eV attributed to adsorbed O_2 or moisture [46,47]. This evolution reveals the emergence of oxidized copper species, absent in the pre-carbonized sample, along with oxygen-containing surface functionalities generated during pyrolysis.

Despite the very low atomic percentage of Cu in the pre-carbonized sample, the Cu 2p spectrum (Fig. 8(c)) still exhibits the characteristic Cu-$2p_{3/2}$ and Cu-$2p_{1/2}$ features [48]. The Cu-$2p_{3/2}$ peak can be satisfactorily fitted with a single component at ~933.4 eV, which is most likely associated with oxidized copper species (Cu_xO). After carbonization, the intensity of the Cu 2p peaks increases slightly, consistent with the higher Cu atomic percentage detected in the carbon matrix after pyrolysis (Table 2). The Cu 2p spectrum of the carbonized samples again displays the Cu-$2p_{3/2}$ and Cu-$2p_{1/2}$ doublet; however, each component now requires two sub-peaks for an adequate fit, revealing the coexistence of both metallic copper (Cu^0) and oxidized copper species (Cu_xO). According to literature assignments [46], the peaks at ~932.7 eV and ~952.6 eV correspond to Cu^0, whereas the components at ~933.7 eV and ~954.0 eV are attributed to Cu_xO. The appearance of Cu^0 components at ~932.7 eV and ~952.6 eV in the carbonized sample indicates that copper undergoes partial reduction during pyrolysis, likely promoted by the carbonaceous environment and the oxygen-depleting conditions of the carbonization process.

The degree of graphitic ordering in the two samples was assessed by Raman spectroscopy (Fig. 9). The pre-carbonized Novolac resin exhibits only a very weak, broad hump in the 1200–1600 cm^{-1} region [49], confirming the amorphous, non-graphitic nature of the precursor and the complete absence of any sp^2 carbon ordering prior to pyrolysis. After carbonization at 550 °C, two well-resolved bands emerge: the G band at ~1582 cm^{-1}, symbolizing the presence of graphitic-like layers (in line with increase of C—C bonds in C1s spectra) and the D band at ~1357 cm^{-1}, associated with structural disorder and defects. The D band intensity is directly related to the density of aromatic sp^2 bonds located at defect sites [50]. The I_D/I_G ratio close to unity indicates a turbostratic, defect-rich carbon structure. A fully graphitic material would exhibit a suppressed D band and a collapsed micropore network; the high D band intensity observed here confirms that the carbonization temperature of 550 °C has been deliberately selected to produce a disordered sp^2 carbon matrix that preserves the defect-rich microporous architecture.

Taken together, the OEA, XPS, and Raman data provide a fully consistent picture of the carbonization process: pyrolysis at 550 °C converts the oxygen- and hydrogen-rich Novolac precursor into a predominantly sp^2 carbon matrix through dehydrogenation and condensation reactions.

The CMSMs integrated in the reactor were prepared following the same protocol as the membrane characterised in our previous work [28], but they were not individually characterised by permeation tests before the catalytic experiments. Their separation performance were therefore assumed to be comparable to that previously reported. Since the properties of carbon molecular sieve membranes are sensitive to the synthesis conditions, future work will address the batch-to-batch

Table 2
Elemental composition of Novolac-based unsupported membrane samples before and after carbonization at 550 °C acquired via Organic Elemental Analysis (OEA) and X-ray Photoelectron Spectroscopy (XPS) and expressed in weight percentages (wt%) and atomic percentages (at.%), respectively.

Sample type	OEA wt%				XPS at.%			
	N	C	H	O	C	O	N	Cu
Pre-carbonization	4.65	73.88	6.72	14.72	74.36	22.34	3.26	0.03
Post-carbonization	0.92	92.02	3.28	3.77	93.90	5.50	0.40	0.20

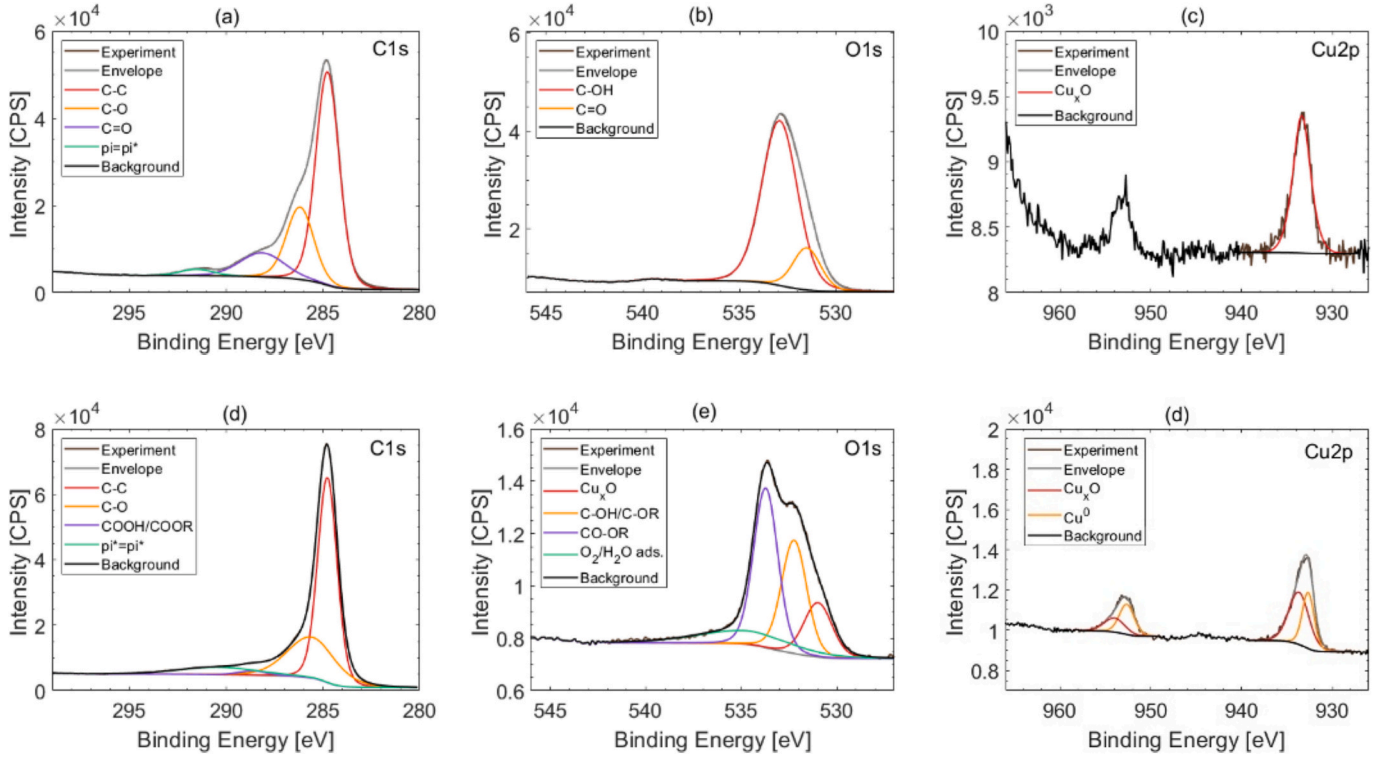

Fig. 8. XPS spectra of pre-carbonized unsupported membrane sample of (a) Carbon, (b) Oxygen, (c) Copper and post-carbonized unsupported membrane sample of (d) Carbon, (e) Oxygen, (f) Copper.

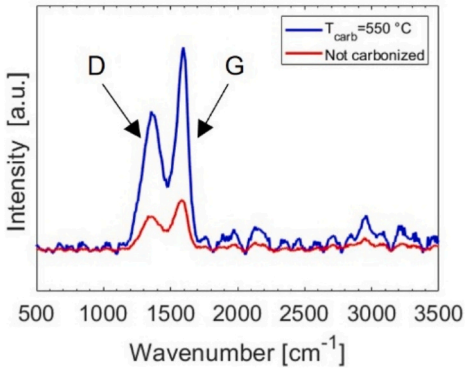

Fig. 9. Raman spectra of pre-carbonized and post-carbonized Novolac-based unsupported membrane samples.

reproducibility of the membrane preparation and the characterization of each membrane before its integration in the reactor.

3.4. POCS geometry comparison in a conventional reactor: Gyroid vs. BCC performances

Prior to membrane reactor testing, the intrinsic catalytic performance of the two POCS geometries – Gyroid and BCC - was systematically assessed in the absence of membranes under two distinct space velocity conditions: WHSV = 715 mLn g_{cat}^{-1} h^{-1}, consistent with the operating window employed in our previous single-membrane reactor study [28], and WHSV = 3285 mLn g_{cat}^{-1} h^{-1} at higher throughput. All experiments were conducted with an under stoichiometric H_2:N_2 = 2:1 molar feed ratio, across a temperature range of 350–450 °C and at operating pressures of 20–40 bar(g), depending on the condition.

The Ru-based catalyst washcoated onto the POCS supports was activated in situ under a H_2:N_2 = 2:1 molar feed ratio at 30 bar(g). The activation protocol consisted of stepwise heating from ambient temperature to 200, 300, 400 and finally 550 °C, with isothermal holds at each plateau to ensure complete and reproducible reduction of the active phase before cooling to the target reaction temperature.

Under high WHSV conditions (Fig. 10(a)), the NH_3 production rate increases monotonically with temperature at 40 bar(g) for both geometries, reaching values of approximately 8 mmol g_{cat}^{-1} h^{-1} at 40 bar(g) and 450 °C, indicative of operation in a predominantly kinetically-controlled regime in which the system remains appreciably far from thermodynamic equilibrium across the full temperature window investigated. At 30 bar(g), however, a modest but reproducible decline in production rate is observed at 450 °C for both Gyroid and BCC configurations, suggesting that the reduced operating pressure is sufficient to bring the system into closer proximity to the thermodynamic equilibrium limit at elevated temperatures. Under low WHSV conditions (Fig. 10(b)), this behaviour is markedly amplified across all pressures tested. A well-defined maximum in NH_3 production rate is observed at 400 °C, followed by a pronounced decline at 450 °C, a trend that is characteristic of thermodynamic control: the extended catalyst contact time associated with the lower space velocity allows the gas-phase composition to approach the equilibrium conversion, beyond which the increasingly unfavourable thermodynamics at elevated temperatures dominates over any kinetic gains. Collectively, these results demonstrate that the transition from a kinetically-controlled to a thermodynamically-limited regime is governed by the compound effect of WHSV and operating pressure, with reduced pressure accelerating this transition even at conditions of elevated space velocity. The H_2 conversion trends, reported as a function of temperature and pressure for both WHSV conditions in Fig. S.1(a) and Fig. S.1(b) of the Supplementary Material, are fully consistent with the NH_3 production rate behaviour described above. Under high WHSV (Fig. S.1(a)), H_2 conversion increases from approximately 5% at 350 °C to 9–10% at 400 °C, before exhibiting a slight decline at 450 °C (particularly at 30 bar(g)), in agreement with the onset of thermodynamic limitation at lower pressures. Under low WHSV (Fig. S.1(b)), conversion values are substantially

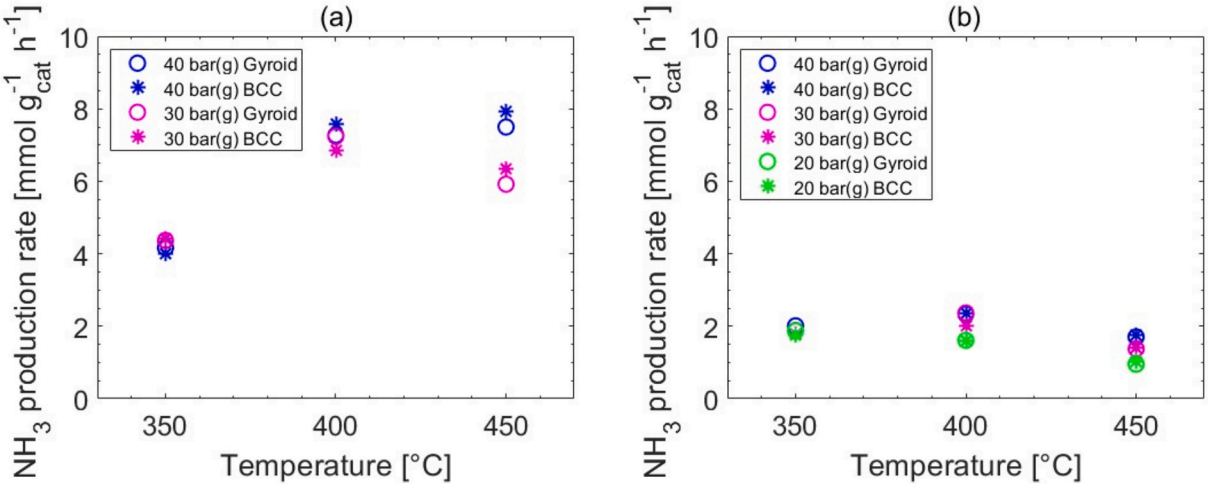

Fig. 10. NH_3 production rate of Gyroid and BCC catalyst structures in a conventional reactor as a function of reaction temperature and pressure: (a) WHSV = 3285 mLn g_{cat}^{-1} h^{-1}; (b) WHSV = 715 mLn g_{cat}^{-1} h^{-1}.

higher, reaching 12–14% at 350–400 °C before declining to 6–11% at 450 °C depending on pressure, with the 20 bar(g) condition exhibiting

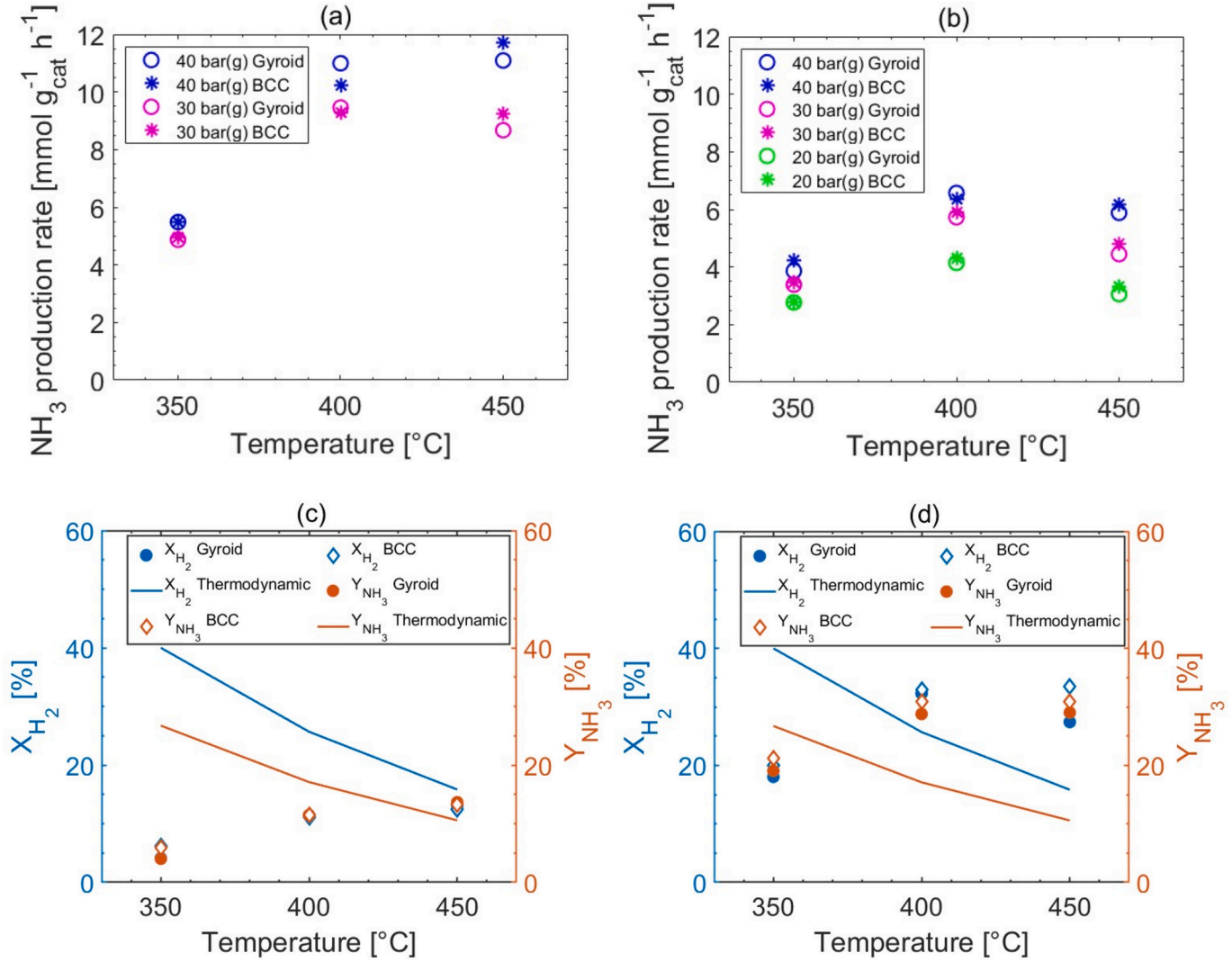

Fig. 11. NH_3 production rate, H_2 conversion and NH_3 yield of Gyroid and BCC catalyst structures in a membrane reactor as a function of reaction temperature: (a) WHSV = 3285 mLn g_{cat}^{-1} h^{-1}, SW = 1, P = 30, 40 bar(g); (b) WHSV = 715 mLn g_{cat}^{-1} h^{-1}, SW = 4, P = 20, 30, 40 bar(g); (c) WHSV = 3285 mLn g_{cat}^{-1} h^{-1}, SW = 1, P = 40 bar(g); (d) WHSV = 715 mLn g_{cat}^{-1} h^{-1}, SW = 4, P = 40 bar(g).

the most pronounced drop, consistent with the equilibrium limit being reached earliest at lower operating pressure. In both regimes, the conversion increases systematically with pressure, reflecting the thermodynamic favourability of NH_3 synthesis at elevated pressures as predicted by Le Chatelier's principle, and decreases with increasing WHSV, as the reduced residence time limits the extent of reaction.

3.5. Membrane reactor enhancement of POCS catalyst structures: Gyroid vs. BCC performances

The same POCS catalyst configurations were subsequently tested in the integrated membrane reactor under the two different WHSV conditions and different sweep gas to feed flow ratio (SW1 and SW4), enabling continuous in-situ removal of ammonia from the reaction side and thus shifting the equilibrium beyond the thermodynamic limit of the conventional system.

Under high WHSV conditions with SW = 1 (Fig. 11(a)), NH_3 production rate increases substantially compared to the conventional case, reaching values of approximately 11 mmol g_{cat}^{-1} h^{-1} at 40 bar(g) and 450 °C, representing a relative enhancement of approximately 50% over the corresponding non-membrane case. Rates increase monotonically with temperature across the full 350–450 °C range, and the physical origin of this trend is clarified by the conversion and yield data in Fig. 11(c). At 350 °C, the experimental H_2 conversion is approximately 5%, against a thermodynamic equilibrium value of approximately 40%, confirming that the high space velocity imposes insufficient contact time for the gas-phase composition to approach equilibrium. As temperature increases toward 450 °C, the experimental conversion rises to approximately 13–14%, representing an approximately 40% relative improvement over the conventional case at the same conditions, and converging toward, but remaining marginally below, the equilibrium value of approximately 15%.

The operative regime shifts fundamentally under low WHSV with SW = 4 (Fig. 11(b)). Although absolute production rates are lower owing to the reduced gas throughput, the H_2 conversion and NH_3 yield (Fig. 11(d)) not only approach but clearly and reproducibly exceed the thermodynamic equilibrium curves at 400 °C and 450 °C. At 400 °C, the experimental H_2 conversion reaches approximately 32%, compared with an equilibrium prediction of approximately 25%, while at 450 °C the experimental conversion of approximately 30–33% stands well above the equilibrium value of approximately 16%. The difference between the Gyroid and BCC structures is more pronounced for the H_2 conversion than for the NH_3 yield (about 6 and 2 percentage points at 450 °C, respectively). The small difference in NH_3 yield is consistent with the slightly higher NH_3 production rate of the BCC structure observed in most of the conventional reactor tests (Fig. 11(b)). The larger deviation in H_2 conversion is instead attributed to experimental uncertainty and to slightly different H_2 losses to the permeate side in the two experiments, since the trans-membrane H_2 flux is included in the calculation of the H_2 conversion (Eq. (4)) but not in that of the NH_3 yield.

Expressed as relative improvements over the corresponding conventional reactor case, these gains correspond to approximately 28% at 400 °C and 100–120% at 450 °C, the enhancement being most pronounced at the highest temperature precisely because the equilibrium conversion is lowest there, making each increment of NH_3 removed by the membrane proportionally more effective in driving the reaction forward. The consequence in terms of production rate is equally evident in Fig. 11(b): the rate maximum previously observed at 400 °C in the conventional tests is substantially attenuated, and production rates remain more sustained toward 450 °C, further evidence of equilibrium displacement by the membrane.

Fig. S.2(a)-(c) report the H_2 conversion and NH_3 yield as a function of temperature for Gyroid and BCC configurations at pressures of 20 and 30 bar(g), compared against the thermodynamic equilibrium curves. At high WHSV (Fig. S2(a)), all experimental values lie below the thermodynamic equilibrium across the full temperature range, confirming kinetically-controlled operation at this space velocity, with the sole exception of the BCC NH_3 yield at 450 °C, which marginally exceeds the equilibrium curve. This apparent exceedance should be interpreted with caution because the NH_3 yield and H_2 conversion are calculated using different material-balance definitions. The NH_3 yield is based on the total ammonia production, whereas the H_2 conversion is based on the net hydrogen balance, including hydrogen consumed by reaction, hydrogen leaving through the retentate and permeate streams, and any hydrogen back-permeation. Therefore, NH_3 transport through the membrane can increase the reported ammonia yield by reducing the ammonia partial pressure on the reaction side, while simultaneous hydrogen transport can modify the net hydrogen-consumption term used to calculate x_{H_2}. At low WHSV and 30 bar(g) (Fig. S2(b)), the conversion and yield values approach and in some cases NH_3 yield surpasses the equilibrium curves. At lower pressures of 20 bar(g) under low WHSV (Fig. S2(c)), the approach to equilibrium is progressively reduced relative to the 30–40 bar(g) case, as the lower operating pressure weakens the transmembrane NH_3 partial pressure gradient and therefore limits the extent of equilibrium displacement achievable by the membrane.

As observed in the conventional reactor benchmarking reported in Section 3.4, not significant difference in NH_3 production rate, H_2 conversion, or NH_3 yield is detected between the Gyroid and BCC geometries under membrane reactor operation across any of the conditions investigated. This geometry-independence under reactive membrane conditions further confirms that both POCS architectures deliver equivalent catalytic performance because the system operates in a regime governed by intrinsic reaction kinetics and thermodynamics rather than by geometry-dependent heat or mass transfer resistances. Consequently, the complete BCC dataset is reported in the Supplementary Material, and the following discussion focuses exclusively on the Gyroid geometry.

3.6. Effect of sweep gas configuration and pressure on membrane reactor performance

To isolate and quantify the individual and combined contributions of space velocity, operating pressure, and sweep configuration on the membrane reactor performance, the Gyroid geometry is analysed in detail in this section. Fig. 12(a) presents a direct comparison between conventional and membrane reactor operation under two WHSV conditions at P = 40 bar(g) with SW = 1. At low WHSV, the membrane enhancement is already clearly established across the entire temperature range, with the membrane system consistently outperforming the conventional reactor. At high WHSV, the benefit is equally pronounced: production rates increase by approximately 35% and 47% at 400 and 450 °C, respectively, relative to the conventional baseline, with the enhancement growing with temperature as the thermodynamic driving force for NH_3 removal intensifies. Reducing the operating pressure to 30 bar (Fig. 12(b)) at high WHSV still yields a visible membrane benefit, with production rate increments of approximately 35% and 45% at 400 and 450 °C, respectively, confirming that the equilibrium-shift effect of the membrane persists across the explored pressure range. The recovery factor is plotted on the secondary axis of Fig. 12(b) and remains in the range of approximately 35–40% across all conditions, with 40 bar(g) operation producing a marginally higher recovery than 30 bar(g) owing to the greater transmembrane partial pressure gradient driving NH_3 permeation. This higher recovery directly translates into a higher total ammonia production rate on the permeate side, confirming that operating pressure is an effective lever for maximising the membrane contribution. The corresponding trends for the BCC geometry are provided in Supplementary Material (Fig. S.3).

The reactant loss and co-feeding behaviour, quantified as the net molar imbalance of H_2 and N_2 between retentate inlet and outlet and reported in Fig. 12(c), provides important additional insight into the

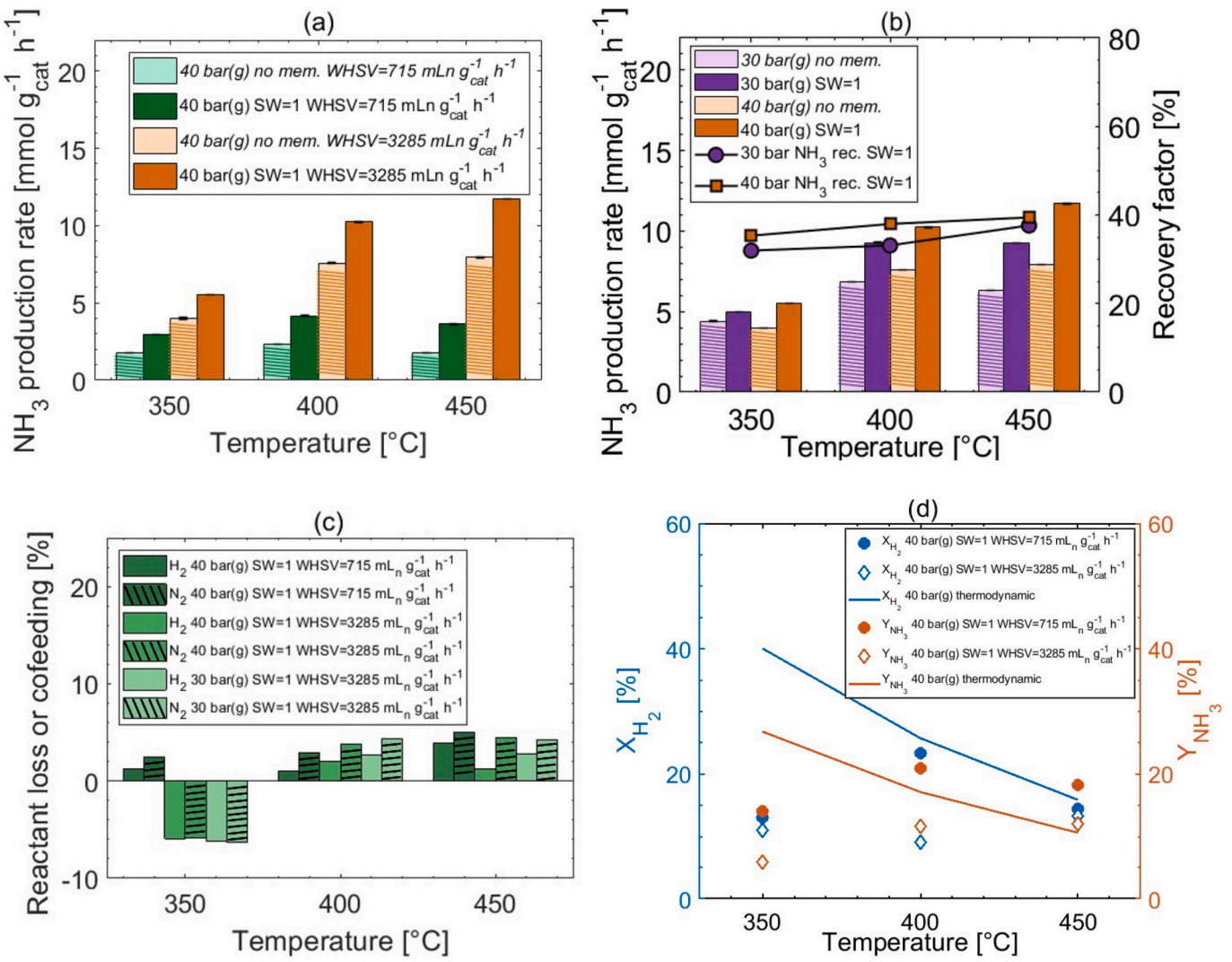

Fig. 12. NH_3 production rate and NH_3 recovery factor of Gyroid catalyst structures as a function of temperature: comparison between conventional and membrane reactor at SW = 1 (a) Effect of WHSV at P = 40 bar(g); (b) Effect of operating pressure at WHSV = 3285 mLn g_{cat}^{-1} h^{-1}, with NH_3 recovery factor reported on the secondary axis; (c) Effect of WHSV on reactant loss or cofeeding at P = 30, 40 bar(g); (d) Effect of WHSV on H_2 conversion and NH_3 yield at P = 40 bar(g).

selectivity of the membrane and the internal consistency of the mass balance. Positive values indicate net permeation of reactants from the retentate to the permeate side (reactant loss), while negative values indicate co-feeding, whereby reactants present in the sweep stream enter the retentate side through the membrane in the direction opposing the desired NH_3 flux. At low temperatures and high WHSV, the reactant loss is slightly negative (indicating co-feeding) which is physically consistent with the low NH_3 partial pressure generated at high space velocity and low temperature, where the driving force for NH_3 permeation is limited. The N_2 loss is systematically higher than the H_2 loss across all conditions, a consequence of the under stoichiometric H_2:N_2 = 2:1 feed ratio employed in this study: the higher N_2 partial pressure in the retentate relative to H_2 creates a larger transmembrane driving force for N_2 permeation, while the lower H_2 partial pressure reduces the tendency for H_2 to permeate. At 400 °C, the reactant loss increases relative to 350 °C, and the low WHSV condition exhibits a higher reactant loss than the high WHSV case, which is directly consistent with the higher conversion achieved at low WHSV (Fig. 12(d)). At 450 °C, this behaviour is reversed: the high WHSV condition exhibits a slightly lower reactant loss than the low WHSV case, particularly for H_2 at 40 bar(g). This reversal is reflected in the convergence of the conversion values between the two WHSV conditions at 450 °C, as the low WHSV system approaches equilibrium and its conversion begins to track that of the high WHSV case.

The conversion and yield data, compared against the thermodynamic equilibrium curves in Fig. 12(d), corroborate these observations. The low WHSV condition approaches the equilibrium conversion more rapidly with increasing temperature than the high WHSV case, and at 400 °C the NH_3 yield for low WHSV already surpasses the thermodynamic equilibrium value, corresponding to a 17% improvement relative to the conventional reactor at the same conditions. At 450 °C, this yield enhancement grows to approximately 44% for low WHSV, while the H_2 conversion under all conditions converges toward the equilibrium curve, with both WHSV cases approaching comparable values as the thermodynamic constraint becomes the dominant limiting factor. This behaviour is consistent with the reactant-loss data in Fig. 12(c), where the darkest green bars correspond to the low-WHSV condition and are represented at the same time by the filled symbols in Fig. 12(d). The relatively larger positive hydrogen-loss value indicates enhanced hydrogen permeation from the retentate to the permeate side and therefore a reduction in the hydrogen flow remaining in the retentate. Consequently, the net hydrogen-consumption term in the numerator of x_{H_2} is reduced by the hydrogen transferred through the membrane, independently of the amount of NH_3 formed.

The high WHSV yield approaches but does not exceed the equilibrium line, consistent with the more limited contact time and therefore

less complete NH_3 permeation in the high space velocity case. Taken together, Fig. 12(a)-(d) demonstrate that the membrane reactor performance is governed by a coupled interplay between space velocity, operating pressure, and the thermodynamic state of the system. Importantly, all results discussed in this section were obtained under a sweep ratio of SW = 1, but as the transmembrane driving force for NH_3 permeation is directly governed by the NH_3 partial pressure difference between the retentate and permeate sides, increasing the sweep ratio to SW = 4 is expected to further dilute the permeate stream, sustain a larger concentration gradient across the membrane, and therefore amplify the equilibrium displacement effect.

Fig. 13(a) extends the analysis to the low WHSV regime, with a SW = 4, over a wider range of operating pressures (20, 30, and 40 bar(g)). Across all temperatures, the conventional reactor baseline increases modestly with pressure, consistent with the thermodynamic expectation for an equilibrium-limited reaction proceeding with a reduction in the number of moles of gas. The membrane enhancement is consistently present at all pressures and temperatures, and grows noticeably as pressure increases from 20 to 40 bar(g). This pressure dependence arises directly from the transmembrane driving force: at higher retentate-side total pressure, the NH_3 partial pressure increases, enhancing the permeation flux through the CMS membrane and resulting in more efficient NH_3 removal. A non-monotonic temperature dependence is observed in the membrane reactor cases, most prominently at 40 bar(g), where the production rate reaches a maximum at 400 °C and slightly declines at 450 °C. This behaviour reflects the competing effects of reaction kinetics and thermodynamics: at 350 °C, slow kinetics limit conversion; at 400 °C, sufficiently fast kinetics combine with effective membrane removal to maximise productivity; at 450 °C, the unfavourable shift of the exothermic equilibrium lowers the thermodynamic, partially offsetting the kinetic gain even in the presence of the membrane. The BCC analysis shows the same overall trend (Fig. S.4). Fig. 13 (b) isolates the effect of sweep gas ratio at fixed operating conditions (P = 40 bar(g), low WHSV), comparing SW = 1 and SW = 4 against the conventional case. Increasing the sweep ratio from 1 to 4 yields a substantial enhancement in NH_3 production rate across all temperatures, with the largest absolute gain observed at 400 °C. This confirms that the permeate-side NH_3 partial pressure, governed by the sweep flow rate, is the primary rate-limiting factor for membrane-assisted equilibrium displacement under these conditions, and that further optimisation of sweep gas utilisation represents the most impactful lever for improving membrane reactor performance. Crucially, the recovery factor reported on the secondary axis of Fig. 13(b) reveals that the benefit of a higher sweep ratio extends beyond the reaction side: SW = 4 not only increases the production rate in the retentate but simultaneously raises the NH_3 recovery to the permeate side to approximately 75–80%, compared with approximately 55–60% at SW = 1.

The H_2 conversion and NH_3 yield data, shown in Fig. 13(c) as a function of temperature across the three pressure conditions at SW = 4, provide quantitative confirmation of the pressure dependence observed in the production rate data. Both parameters increase systematically with operating pressure at all temperatures, consistent with the

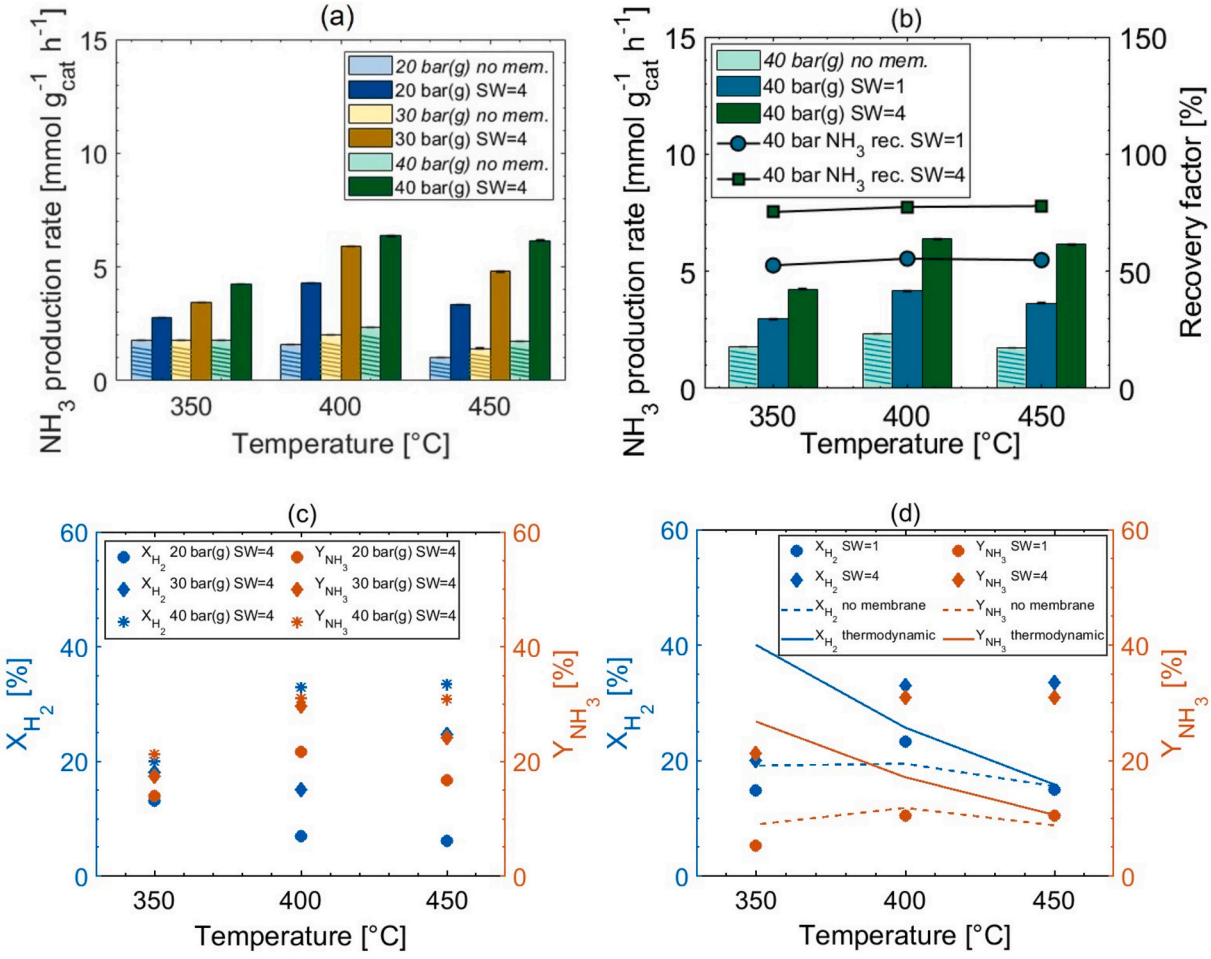

Fig. 13. NH_3 production rate, H_2 conversion and NH_3 yield of Gyroid catalyst structures as a function of temperature at WHSV = 715 mLn g_{cat}^{-1} h^{-1}: (a) effect of operating pressure at SW = 4; (b) effect of sweep gas ratio at P = 40 bar(g), with NH_3 recovery factor reported on the secondary axis; (c) H_2 conversion and NH_3 yield as a function of operating pressure at SW = 4; (d) H_2 conversion and NH_3 yield at P = 40 bar(g), comparing SW = 1, SW = 4, the conventional membrane-free case, and the thermodynamic equilibrium limit.

thermodynamic favourability of NH_3 synthesis at elevated pressures. The conversion improvement between 20 and 40 bar(g) is most pronounced at 400 and 450 °C, where the system is thermodynamically most sensitive to pressure, while at 350 °C the kinetic limitation constrains conversion regardless of pressure and the differences between conditions are correspondingly smaller. Fig. 13(d) provides the most complete picture of the membrane contribution by comparing, at 40 bar (g), the H_2 conversion and NH_3 yield achieved under SW = 1, and SW = 4 conditions against both the calculated thermodynamic equilibrium curves and the conventional case. At 350 °C, none of the membrane configurations exceeds the thermodynamic equilibrium. Nevertheless, SW = 4 already delivers an ammonia yield improvement of approximately 136% relative to the conventional case at 350 °C, while SW = 1 remains closer to the conventional case. At 400 °C, the divergence between SW = 1 and SW = 4 becomes dramatically more pronounced. The SW = 4 condition achieves an H_2 conversion improvement of approximately 65% and an NH_3 yield improvement of approximately 170% relative to the conventional reactor, with both metrics clearly surpassing not only the conventional case but also the thermodynamic equilibrium curve. By contrast, SW = 1 at 400 °C remains marginally below the thermodynamic equilibrium and performs in close proximity to the conventional reactor, confirming that a sweep ratio of unity is insufficient to generate the permeate-side concentration gradient necessary to drive the system beyond its thermodynamic limit. At 450 °C, the thermodynamic equilibrium conversion and yield both decrease causing all curves to converge toward lower absolute values. In this regime, the conventional reactor and SW = 1 membrane reactor approach the equilibrium boundary from below, while the SW = 4 condition continues to track the same equilibrium trend established at 400 °C, maintaining both conversion and yield above the thermodynamic limit. The fact that Y_{NH_3} is lower than x_{H_2} under the SW = 4 condition is consistent with the lower reactant loss observed at the higher sweep ratio. With less H_2 and N_2 transferred through the membrane, the measured streams are less affected by reactant permeation and back-permeation. Consequently, the calculated hydrogen conversion more directly reflects the net hydrogen balance, whereas the ammonia yield remains based on the ammonia formed and the effective hydrogen input.

3.7. Influence of transmembrane ΔP on membrane reactor performance

The transmembrane pressure difference (ΔP) represents a critical additional degree of freedom in the optimisation of membrane reactor operating conditions, as it directly governs the convective contribution to the total NH_3 permeation flux. It is important to note, however, that the applicable range of ΔP in this study was subject to a significant experimental constraint arising from the high permeance and low selectivities of the CMS membrane employed. When a positive transmembrane pressure difference is imposed, the high membrane permeability induces rapid permeation of all gas species from the retentate to the permeate zone, generating a sharp pressure drop on the reaction side until the two pressures equilibrate [51]. To maintain stable operation and preserve the desired ΔP throughout each experiment, it was necessary to operate at the highest space velocity condition used in this study (WHSV = 3285 mLn g_{cat}^{-1} h^{-1}), as the elevated feed flow rate provides a sufficient and continuous gas supply to the retentate zone to compensate for the permeation losses through the membrane and sustain the imposed pressure differential. For the same reason, and additionally owing to the flow rate limitations of the mass flow controllers available in the experimental setup, the transmembrane pressure difference study was conducted exclusively under SW = 1 conditions.

Fig. 14(a) shows that at ΔP = 0 bar, the membrane reactor consistently outperforms the conventional baseline across all temperatures, across the entire temperature range investigated, confirming the equilibrium-shift benefit of diffusion-driven NH_3 removal through the CMS membrane in the absence of any convective driving force. As ΔP increases from 0 to 3 bar, however, the NH_3 production rate decreases monotonically, and at ΔP = 3 bar it falls to values comparable to, or marginally below, the conventional reactor at 350 °C. This counterintuitive trend is attributed to the NH_3/H_2 and NH_3/N_2 non-ideal selectivity of the CMS membrane: while a positive ΔP enhances convective permeation of NH_3, it simultaneously promotes the loss of H_2 and N_2 reactants to the permeate side, depleting the reactive mixture within the retentate and reducing overall productivity. Fig. 14(b) quantifies this trade-off by reporting the fractional loss of H_2 and N_2 to the permeate side as a function of ΔP and temperature. Consistent with the relative permeance hierarchy of the CMS membrane, the fraction of H_2 lost to the permeate side is systematically higher than that of N_2 across all conditions, a consequence of the smaller kinetic diameter of H_2 (0.289 nm) relative to N_2 (0.364 nm). At ΔP = 3 bar, this non-selective convective permeation becomes severe: H_2 losses approach 100% and N_2 losses reach approximately 90%, implying that the vast majority of the reactants introduced into the retentate zone permeate through the membrane before they can participate in the catalytic synthesis reaction. The resulting stoichiometric depletion and severe imbalance of the reactive mixture in the retentate constitutes the primary cause of the NH_3 production rate decline observed in Fig. 14(a). Taken together, Fig. 14(a)-(b) demonstrate that, for CMS membranes of the permeance and selectivity characteristics employed in this study, operation at ΔP = 0 represents the optimal strategy for maximising membrane reactor performance. For the BCC analysis, these tests were performed at a single pressure difference to verify whether the same trend held, and this was indeed the case: because the membrane properties were identical, the best results were again obtained at ΔP = 0 (Fig. S.5).

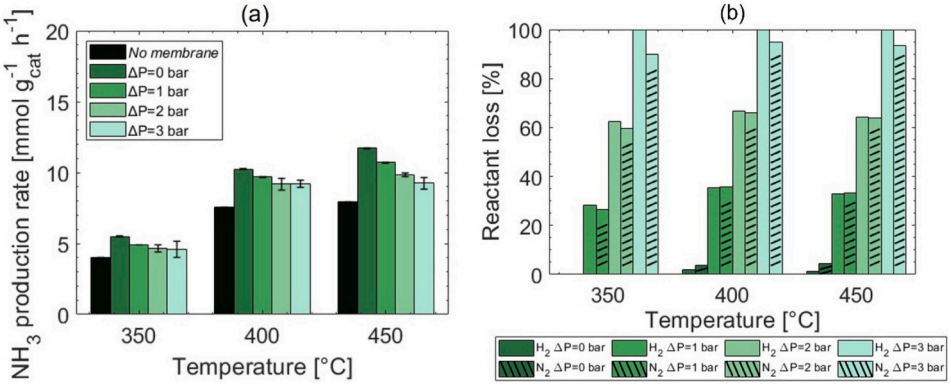

Fig. 14. Effect of transmembrane pressure difference on the performance of Gyroid catalyst structures in a membrane reactor: (a) NH_3 production rate as a function of reaction temperature; (b) Fractional loss of H_2 and N_2 reactants to the permeate side as a function of reaction temperature. WHSV = 3285 mLn g_{cat}^{-1} h^{-1}, SW = 1, P = 40 bar(g), ΔP = 0–3 bar.

3.8. Scaling the reactor configuration: one versus four membrane reactor configurations

This section compares the single- and four-membrane reactor configurations. Moving from one to four CMSMs, both the membrane area and the catalyst mass were increased, with a similar catalyst quantity per membrane. The comparison therefore evaluates the combined effect of membrane area and catalyst loading on the total NH_3 production rate, membrane-area-normalised productivity, and NH_3 recovery factor. It should not be interpreted as an isolated assessment of membrane-area scaling. The analysis further examines whether the four-membrane configuration provides a proportional productivity benefit relative to the additional membrane area and catalyst deployed.

Fig. 15(a) reports the catalyst-normalised NH_3 production rate at SW = 4 across the full pressure range (P = 20, 30, and 40 bar(g)), comparing the single and four membrane configurations. The benefit of increasing the membrane number is clearly visible across the entire temperature range and at all pressures investigated. However, because the four-membrane configuration also contains a proportionally larger catalyst inventory, its higher productivity reflects the combined effects of increased catalytic capacity and membrane area rather than membrane scaling alone. The relative gain is most pronounced at 350 °C and decreases progressively with increasing temperature. At higher temperatures, the intrinsic reaction rate increases for both configurations, and both progressively approach the same thermodynamic equilibrium. As a result, the relative benefit of adding both catalyst and membrane area decreases, and the catalyst-normalised productivities become more similar. The reduced marginal gain at higher temperature therefore reflects the increasing importance of the thermodynamic limitation, although the individual contributions of catalyst loading and membrane area cannot be separated from the present comparison. For the BCC geometry, experiments were conducted only at 40 bar(g), yet the same qualitative trend was retained, with the four-membrane configuration outperforming the single-membrane case in terms of productivity (Fig. S.6).

Fig. 15(b) extends the analysis by reporting the NH_3 production rate normalised by the total active membrane area, across the full pressure range. For each pressure condition, the membrane-area-normalised productivity is consistently and substantially higher for the four membrane configuration than for the single membrane over the investigated temperature range. Interpreting this result requires accounting for the fact that the two configurations differ not only in membrane number but also in catalyst mass, corresponding to a similar catalyst quantity per membrane. The higher area-normalised productivity of the four-membrane configuration therefore reflects the combined effect of the additional catalyst and membrane area, as well as their interaction within the integrated reactor. The larger catalyst inventory increases the total NH_3 formation capacity, while the larger membrane area increases the overall NH_3-removal capacity and can help maintain the trans-membrane NH_3 concentration gradient. These coupled effects can enhance the reaction-permeation interaction and produce a higher productivity per unit membrane area. However, the present comparison does not allow the separate contributions of catalyst loading and membrane area to be quantified, because both parameters are changed simultaneously.

The results demonstrate that scaling the integrated configuration from one to four membrane elements remains beneficial under the investigated conditions. They are consistent with a substantial contribution from reaction-permeation coupling, but they do not by themselves prove that the system is exclusively reaction-limited rather than permeation-limited. Separating these regimes would require additional experiments or simulations in which catalyst mass and membrane area are varied independently. The membrane-area-normalised productivity increases with temperature and pressure in both configurations, consistent with the higher reaction rates and stronger NH_3 partial pressure driving forces obtained at more severe operating conditions.

Table 3 quantifies these trends comprehensively, reporting both the percentage improvement in membrane-area-normalised NH_3 productivity and the NH_3 recovery factor upon increasing the membrane number from one to four across all explored conditions. At P = 20 bar(g) and SW = 4, the improvement in areal productivity reaches 281.8% at 350 °C, decreasing to 148.2% at 400 °C and 45.3% at 450 °C. The

Table 3
Percentage improvement in membrane-area-normalised NH_3 productivity and NH_3 recovery factor upon increasing the number of membranes from 1 to 4, as a function of temperature, pressure, and sweep ratio. WHSV = 715 mLn g_{cat}^{-1} h^{-1}.

T [°C]	P [bar]	SW [–]	Improvement of membrane-area-normalised NH_3 productivity [%]	Recovery factor [%]
350	20	4	281.8	51.9–70.3
400			148.2	43.5–72.4
450			45.3	43.6–72.1
350	30	4	285.6	68.6–72.9
400			192.0	59.7–75.6
450			74.6	59.1–74.73
350	40	4	423.7	89.7–75.3
400			165.1	89.8–77.5
450			64.6	89.7–77.8

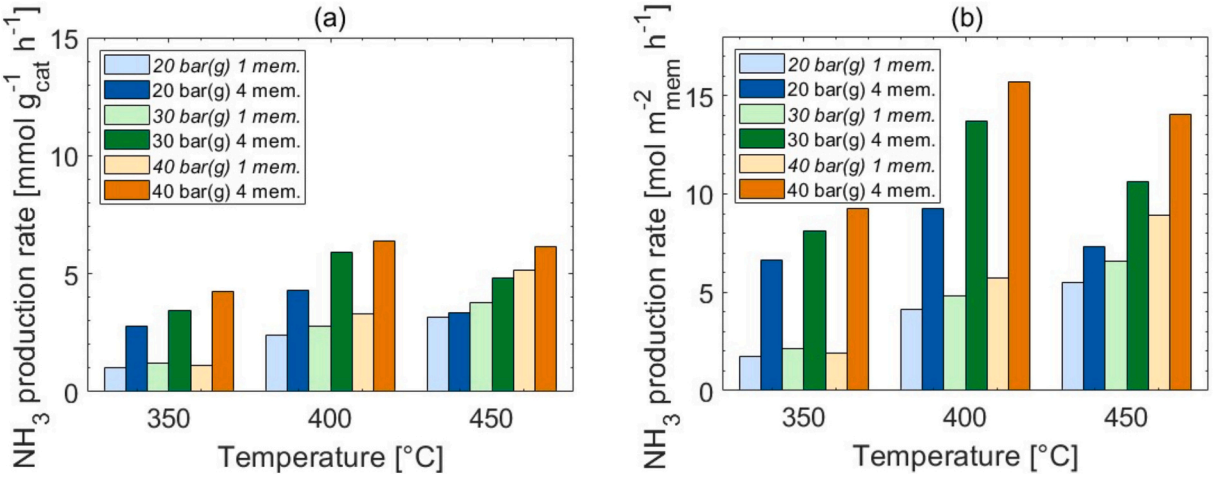

Fig. 15. NH_3 production rate of Gyroid catalyst structures as a function of reaction temperature: effect of scaling the number of membranes from 1 to 4: (a) Effect of pressure on catalyst-normalised productivity; (b) Membrane-area-normalised NH_3 productivity at P = 20, 30, 40 bar(g). SW = 4, WHSV = 715 mLn g_{cat}^{-1} h^{-1} for all conditions.

corresponding recovery factor increases from 51.9% to 70.3% at 350 °C and from 43.6% to 72.4% at higher temperature. At $P = 30$ bar(g), comparable improvement values are observed: 285.6%, 192.0%, and 74.6% at 350, 400, and 450 °C, respectively, while the recovery factor is notably more stable, ranging between 59.1% and 75.6% and varying by less than 15 percentage points across the full temperature range. This thermal stability of the recovery factor is particularly significant: it indicates that the four membrane configuration maintains a consistently high NH_3 extraction efficiency across the entire thermal operating window. At $P = 40$ bar(g), the higher total pressure amplifies both the NH_3 partial pressure in the retentate and the transmembrane driving force. The area-normalised productivity improvement is therefore the largest among the investigated pressure conditions, reaching 423.7% at 350 °C and declining to 165.1% and 64.6% at 400 and 450 °C, respectively. Correspondingly, the recovery factor at 40 bar(g) is the highest of all pressure conditions, ranging from approximately 89.7 to 77.8% across the temperature range.

The consistent decrease in the productivity improvement with increasing temperature can be interpreted as a diminishing relative benefit of scaling the integrated configuration. At higher temperatures, the single-membrane configuration already achieves higher reaction rates and captures a larger fraction of the available NH_3 flux. Consequently, the additional catalyst and membrane elements provide a smaller relative improvement than at 350 °C. This trend supports the conclusion that the four-membrane configuration is most advantageous under the lower-temperature conditions investigated, while the separate contributions of membrane area and catalyst loading cannot be isolated from the present dataset.

4. Conclusions

This work demonstrates, for the first time, the integration of a scaled-up multi-membrane reactor for ammonia synthesis combining four tubular carbon molecular sieve membranes (CMSMs) with two complementary 3D-printed metallic Periodic Open Cellular Structure (POCS) geometries (Gyroid and Body-Centred Cubic (BCC)) manufactured in Inconel 625 by Laser Powder Bed Fusion and activated with a Ru-based catalyst. The study advances the state of the art in dual process intensification for ammonia synthesis from TRL 3–4 to TRL 5, with the catalyst inventory and membrane area scaled approximately in proportion with respect to our previous laboratory-scale proof of concept. The dip-spin coating protocol, previously optimised on smaller Gyroid supports, was successfully transferred to the larger scale and applied without modification to both POCS topologies; the larger support volume required an increased number of coating cycles to reach the higher target loading, with optical microscopy confirming the absence of cracking and delamination. The carbon molecular sieve membranes (CMSMs) were produced and characterised by organic elemental analysis, XPS, and Raman spectroscopy. Carbonization at 550 °C was confirmed to convert the oxygen- and hydrogen-rich Novolac precursor into a predominantly sp^2 carbon matrix through dehydrogenation and condensation reactions. XPS additionally confirmed the partial reduction of Cu^{2+} to Cu^0 during pyrolysis and the survival of thermally stable carbonyl and CuO_x surface groups in the final membrane.

Baseline testing in the conventional reactor, conducted over a temperature range of 350–450 °C and pressures of 20–40 bar(g), demonstrated that the Gyroid and BCC POCS configurations deliver virtually identical catalytic performance under all explored conditions. At high WHSV, NH_3 production rates increase monotonically with temperature at 40 bar(g), consistent with kinetically-controlled operation, while a slight decline at 450 °C under 30 bar(g) signals the onset of thermodynamic limitation at lower pressure. At low WHSV, this thermodynamic limit is more clearly exposed at 400 °C.

Upon integration of the CMSMs into the membrane reactor, the same geometry-independence was confirmed. The membrane consistently enhanced NH_3 production rates relative to the conventional baseline across all operating conditions. At high WHSV with SW = 1, production rate improvements of approximately 35–47% were achieved at 400–450 °C and 30–40 bar(g), with the 40 bar(g) condition delivering a marginally higher NH_3 recovery factor owing to the stronger transmembrane partial pressure gradient. However, super-equilibrium operation, in which both H_2 conversion and NH_3 yield exceeded the thermodynamic equilibrium curves, was achievable exclusively at low WHSV with SW = 4. Under these conditions, the H_2 conversion exceeded the thermodynamic equilibrium limit by about 30% at 400 °C and 110% at 450 °C. At the same temperature, NH_3 yield increased by 65% and 170% relative to equilibrium, respectively, indicating that SW = 4 is the critical operating condition needed to unlock the full equilibrium-displacement potential of the POCS-CMSM membrane reactor system. The systematic investigation of sweep gas ratio revealed also that increasing SW from 1 to 4 not only amplifies the NH_3 production rate but simultaneously raises the NH_3 recovery factor to approximately 75–80%, compared with 55–60% at SW = 1, confirming that permeate-side dilution of NH_3 is the primary lever governing the strength of equilibrium displacement.

Finally, the direct comparison between the single-membrane and four-membrane reactor configurations demonstrated clear and systematic performance improvements under all investigated conditions. The membrane-area-normalised NH_3 productivity was consistently higher in the four-membrane configuration than for the single-membrane case. Because the four-membrane configuration also contains a proportionally larger catalyst inventory, this improvement reflects the combined effects of increased membrane area, catalyst loading, and their interaction within the integrated reactor. The results therefore demonstrate the benefit of scaling the complete membrane-reactor configuration, but do not allow the individual contributions of membrane area and catalyst mass to be separated or conclusively establish a purely reaction-limited regime. The largest absolute improvement was recorded at 350 °C and 40 bar(g), where the membrane-area-normalised productivity increased by 423.7% relative to the single-membrane baseline.

CRediT authorship contribution statement

I. Gargiulo: Writing – original draft, Investigation, Formal analysis, Conceptualization. **A. Vita:** Writing – review & editing, Investigation, Conceptualization. **C. Italiano:** Investigation. **C. Coiana:** Investigation. **F. Gallucci:** Writing – review & editing, Supervision, Funding acquisition, Conceptualization.

Declaration of competing interest

The authors declare that they have no known competing financial interests or personal relationships that could have appeared to influence the work reported in this paper.

Acknowledgement

“Funded by the European Union (grant agreement No 101058565, AMBHER project). Views and opinions expressed are however those of the author(s) only and do not necessarily reflect those of the European Union. Neither the European Union nor the granting authority can be held responsible for them”.

The authors would like to thank ENGIE for supplying the bare 3D printed supports, Jonhson Matthey for supplying the catalyst powders and TECNALIA for supplying the membranes, as part of the AMBHER project. The authors would also like to thank Pranav Arun for conducting the Raman analyses, Riccardo Ferretti for assistance with OEA analysis, and Joris Garenfeld for his contributions to the design and construction of the reactor.

Appendix A. Supplementary data

Supplementary data to this article can be found online at https://doi.org/10.1016/j.cej.2026.183234.

Data availability

Data will be made available on request.

References

[1] CO2 Emissions – Global Energy Review 2025 – Analysis - IEA, (n.d.). https://www.iea.org/reports/global-energy-review-2025/co2-emissions (accessed May 13, 2026).

[2] H. Ritchie, P. Rosado, Electricity Mix, Our World in Data. https://ourworldindata.org/electricity-mix, 2020 (accessed March 20, 2026).

[3] A. Saletnik, B. Saletnik, C. Puchalski, Coal as the world's dominant energy source and its role in the energy transformation and regulations of European Green Deal, J. Environ. Manag. 392 (2025) 126815, https://doi.org/10.1016/j.jenvman.2025.126815.

[4] Renewable Energy Explained - Types and Usage U.S. Energy Information Administration (EIA), (n.d.). https://www.eia.gov/energyexplained/renewable-sources/types-and-usage.php (accessed March 20, 2026).

[5] R. Bhandari, N. Adhikari, A comprehensive review on the role of hydrogen in renewable energy systems, Int. J. Hydrog. Energy 82 (2024) 923–951, https://doi.org/10.1016/j.ijhydene.2024.08.004.

[6] B. Reda, A.A. Elzamar, S. AlFazzani, S.M. Ezzat, Green hydrogen as a source of renewable energy: a step towards sustainability, an overview, Environ. Dev. Sustain. 27 (12) (2024) 29213–29233, https://doi.org/10.1007/s10668-024-04892-z.

[7] A. Chaube, A. Chapman, Y. Shigetomi, K. Huff, J. Stubbins, The role of hydrogen in achieving long term Japanese energy system goals, Energies 13 (2020) 4539, https://doi.org/10.3390/EN13174539.

[8] D.K. Madheswaran, S. Vengatesan, S. Jegadheeswaran, M. Thangamuthu, H. Togun, B. Duraisamy, C. Ouyang, M.W. Khan, Ammonia as a hydrogen carrier: a comprehensive analysis of electrolysis efficiency and its potential in sustainable energy systems, Renew. Sust. Energ. Rev. 221 (2025), https://doi.org/10.1016/j.rser.2025.115915.

[9] A. Kozuch, K. Adamowicz, A.G. Capodaglio, Developments and issues in renewable ecofuels and feedstocks, Energies 17 (2024) 3560, https://doi.org/10.3390/EN17143560.

[10] Executive Summary – Ammonia Technology Roadmap – Analysis IEA, (n.d.). https://www.iea.org/reports/ammonia-technology-roadmap/executive-summary (accessed June 14, 2026).

[11] K.H.R. Rouwenhorst, P.M. Krzywda, N.E. Benes, G. Mul, L. Lefferts, Ammonia production technologies, Techno-Econ. Chall. Green Ammonia Energ. Vector (2021) 41–83, https://doi.org/10.1016/B978-0-12-820560-0.00004-7.

[12] G.R. Maxwell, Synthetic Nitrogen Products: A Practical Guide to the Products and Processes, Springer, 2004.

[13] C. Smith, A.K. Hill, L. Torrente-Murciano, Current and future role of Haber–Bosch ammonia in a carbon-free energy landscape, Energy Environ. Sci. 13 (2020) 331–344, https://doi.org/10.1039/C9EE02873K.

[14] J. Zhang, X. Li, J. Zheng, M. Du, X. Wu, J. Song, C. Cheng, T. Li, W. Yang, Non-thermal plasma-assisted ammonia production: a review, Energy Convers. Manag. 293 (2023), https://doi.org/10.1016/j.enconman.2023.117482.

[15] D.K. Babi, P. Lutze, J.M. Woodley, R. Gani, A process synthesis-intensification framework for the development of sustainable membrane-based operations, Chem. Eng. Process. Process Intensif. 86 (2014) 173–195, https://doi.org/10.1016/J.CEP.2014.07.001.

[16] A. Basile, S. Liguori, A. Iulianelli, Membrane Reactors for Ammonia Production, Elsevier Inc., 2015, https://doi.org/10.1016/B978-1-78242-223-5.00002-9.

[17] A. Bhown, E.L. Cussler, Mechanism for selective ammonia transport through poly (vinylammonium thiocyanate) membranes, J. Am. Chem. Soc. 113 (1991) 742–749, https://doi.org/10.1021/JA00003A002.

[18] Y. He, E.L. Cussler, Ammonia permeabilities of perfluorosulfonic membranes in various ionic forms, J. Membr. Sci. 68 (1992) 43–52, https://doi.org/10.1016/0376-7388(92)80148-D.

[19] K. Wakimoto, W.W. Yan, N. Moriyama, H. Nagasawa, M. Kanezashi, T. Tsuru, Ammonia permeation of fluorinated sulfonic acid polymer/ceramic composite membranes, J. Membr. Sci. 658 (2022) 120718, https://doi.org/10.1016/j.memsci.2022.120718.

[20] W.W. Yan, T. Tsuru, Overview: insight into NH3 permselective membranes and their application to a membrane reactor for efficient ammonia production, Sep. Purif. Technol. 370 (2025) 133275, https://doi.org/10.1016/J.SEPPUR.2025.133275.

[21] S. Padinjarekutt, H. Li, S. Ren, P. Ramesh, F. Zhou, S. Li, G. Belfort, M. Yu, Na+-gated nanochannel membrane for highly selective ammonia (NH3) separation in the Haber-Bosch process, Chem. Eng. J. 454 (2023) 139998, https://doi.org/10.1016/J.CEJ.2022.139998.

[22] S. Padinjarekutt, B. Sengupta, H. Li, K. Friedman, D. Behera, R. Lecaros, M. Yu, Synthesis of Na+-gated nanochannel membranes for the ammonia (NH3) separation, J. Membr. Sci. 674 (2023) 121512, https://doi.org/10.1016/J.MEMSCI.2023.121512.

[23] W.W. Yan, K. Wakimoto, N. Moriyama, H. Nagasawa, M. Kanezashi, T. Tsuru, Development of sulfonated (3-Mercaptopropyl)trimethoxysilane membranes with thermal stability and excellent NH3 perm-selectivity at 300 °C, J. Membr. Sci. 696 (2024) 122535, https://doi.org/10.1016/j.memsci.2024.122535.

[24] W.W. Yan, K. Wakimoto, N. Moriyama, H. Nagasawa, M. Kanezashi, T. Tsuru, Fabrication of 3-(trihydroxysilyl)-1-propanesulfonic acid membranes with superior affinity and selectivity for NH3 permeation over H2 and N2 at 50–300°C, J. Membr. Sci. 702 (2024) 122798, https://doi.org/10.1016/j.memsci.2024.122798.

[25] M. Adejumo, L. Oleksy, S. Liguori, Innovative NH3 separation over immobilized molten salt membrane at high temperatures, Chem. Eng. J. 479 (2024) 147434, https://doi.org/10.1016/J.CEJ.2023.147434.

[26] H.J. Li, Y.D. Liu, A review of polymer-derived carbon molecular sieve membranes for gas separation, New Carbon Mater. 37 (2022) 484–507, https://doi.org/10.1016/S1872-5805(22)60613-9.

[27] W.N.W. Salleh, A.F. Ismail, Carbon membranes for gas separation processes: recent progress and future perspective, J. Membr. Sci. Res. 1 (2015) 2–15.

[28] I. Gargiulo, A. Vita, C. Italiano, M.A. Llosa Tanco, D.A. Pacheco Tanaka, F. Gallucci, Activated triply periodic minimal surfaces (TPMS) gyroid supports for efficient ammonia synthesis in membrane-integrated reactors, Int. J. Hydrog. Energy 235 (2026) 155170, https://doi.org/10.1016/J.IJHYDENE.2026.155170.

[29] K.G. Allen, T.W. von Backström, D.G. Kröger, Packed bed pressure drop dependence on particle shape, size distribution, packing arrangement and roughness, Powder Technol. 246 (2013) 590–600, https://doi.org/10.1016/J.POWTEC.2013.06.022.

[30] A. Guardo, M. Coussirat, F. Recasens, M.A. Larrayoz, X. Escaler, CFD study on particle-to-fluid heat transfer in fixed bed reactors: convective heat transfer at low and high pressure, Chem. Eng. Sci. 61 (2006) 4341–4353, https://doi.org/10.1016/J.CES.2006.02.011.

[31] E. Tronconi, G. Groppi, C.G. Visconti, Structured catalysts for non-adiabatic applications, Curr. Opin. Chem. Eng. 5 (2014) 55–67, https://doi.org/10.1016/J.COCHE.2014.04.003.

[32] V. Palma, C. Ruocco, M. Cortese, M. Martino, Recent advances in structured catalysts preparation and use in water-gas shift reaction, Catalysts 9 (2019) 991, https://doi.org/10.3390/CATAL9120991.

[33] P. Gomes, M. Iwaniszyn, Periodic Open Cellular Structures (POCS) as catalyst supports—a review, Energies 15 (2022) 7703, https://doi.org/10.3390/EN15207703.

[34] G. Chouhan, G. Bala Murali, Designs, advancements, and applications of three-dimensional printed gyroid structures: a review, Proc. Inst. Mech. Eng. Part E: J. Process Mech. Eng. 238 (2024) 965–987, https://doi.org/10.1177/09544089231160030.

[35] S. Bai, Y. Hao, Y. Yan, L. Li, P. Cheng, Z. Tu, H. Zhou, L. Cheng, H. Mei, W. Ding, Triply Periodic Minimal Surface (TPMS) structures in 3D-printed catalyst supports: advanced optimization of heat transfer, mass transport, and mechanical stability for catalysis, Adv. Mater. Technol. 11 (2026) e02352, https://doi.org/10.1002/ADMT.202502352.

[36] M. Zhao, F. Liu, G. Fu, D.Z. Zhang, T. Zhang, H. Zhou, Improved mechanical properties and energy absorption of BCC lattice structures with triply periodic minimal surfaces fabricated by SLM, Materials 11 (2018) 2411, https://doi.org/10.3390/MA11122411.

[37] C. Italiano, G. Marino, M. Thomas, B. Hary, S. Nardone, S. Richard, A. Saker, D. Tasso, N. Meynet, P. Olivier, F. Gallucci, A. Vita, Carbon-free H2 production from ammonia decomposition over 3D-printed Ni-alloy structures activated with a Ru/Al2O3 catalyst, Processes 12 (2024) 2663, https://doi.org/10.3390/PR12122663.

[38] C. Italiano, G. Marino, M. Thomas, B. Hary, S. Nardone, S. Richard, A. Saker, D. Tasso, N. Meynet, P. Olivier, F. Gallucci, A. Vita, Combined dip/spin coating deposition of Ni/CeO2 and Ni/CeO2-Al2O3 onto 3D printed AlSi10Mg Periodic Open Cellular Structures (POCS), Appl. Surf. Sci. Adv. 27 (2025) 100731, https://doi.org/10.1016/J.APSADV.2025.100731.

[39] X. Chen, X. Wang, D. Fang, A review on C1s XPS-spectra for some kinds of carbon materials, Fullerenes Nanotubes Carbon Nanostruct. 28 (2020) 1048–1058, https://doi.org/10.1080/1536383X.2020.1794851.

[40] M. Quintana, K. Spyrou, M. Grzelczak, W.R. Browne, P. Rudolf, M. Prato, Functionalization of graphene via 1,3-dipolar cycloaddition, ACS Nano 4 (2010) 3527–3533, https://doi.org/10.1021/NN100883P.

[41] P. Stathi, D. Gournis, Y. Deligiannakis, P. Rudolf, Stabilization of phenolic radicals on graphene oxide: an XPS and EPR study, Langmuir 31 (2015) 10508–10516, https://doi.org/10.1021/ACS.LANGMUIR.5B01248.

[42] J.F. Moulder, W.F. Stickle, P.E. Sobol, K.D. Bomben, Handbook of X-ray Photoelectron Spectroscopy A Reference Book of Standard Spectra for Identification and Interpretation of XPS Data, n.d.

[43] M. Smith, L. Scudiero, J. Espinal, J.S. McEwen, M. Garcia-Perez, Improving the deconvolution and interpretation of XPS spectra from chars by ab initio calculations, Carbon N. Y. 110 (2016) 155–171, https://doi.org/10.1016/J.CARBON.2016.09.012.

[44] T. Kato, Y. Yamada, Y. Nishikawa, H. Ishikawa, S. Sato, Carbonization mechanisms of polyimide: methodology to analyze carbon materials with nitrogen, oxygen, pentagons, and heptagons, Carbon N. Y. 178 (2021) 58–80, https://doi.org/10.1016/j.carbon.2021.02.090.

[45] K. Ishimaru, T. Hata, P. Bronsveld, D. Meier, Y. Imamura, Spectroscopic analysis of carbonization behavior of wood, cellulose and lignin, J. Mater. Sci. 42 (2007) 122–129, https://doi.org/10.1007/s10853-006-1042-3.

[46] A. Roy, A.K. Mukhopadhyay, S.C. Das, G. Bhattacharjee, A. Majumdar, R. Hippler, Surface stoichiometry and optical properties of Cux–TiyCz thin films deposited by

magnetron sputtering, Coatings 9 (2019) 551, https://doi.org/10.3390/COATINGS9090551.
[47] A. Hu, G. Chen, A. Huang, Z. Cai, T. Yang, C. Ma, L. Li, H. Gao, J. Gu, C. Zhu, Y. Wu, X. Qiu, J. Xu, J. Shen, L. Zhong, O-phenylenediamine derived fluorescent carbon quantum dots for detection of Hg(II) in environmental water, J. Fluoresc. 34 (2) (2023) 905–913, https://doi.org/10.1007/S10895-023-03331-Y.
[48] T. Ghodselahi, M.A. Vesaghi, A. Shafiekhani, A. Baghizadeh, M. Lameii, XPS study of the Cu@Cu2O core-shell nanoparticles, Appl. Surf. Sci. 255 (2008) 2730–2734, https://doi.org/10.1016/J.APSUSC.2008.08.110.
[49] D.V. Sivkov, O.V. Petrova, S.V. Nekipelov, A.S. Vinogradov, R.N. Skandakov, S. I. Isaenko, A.M. Ob'edkov, B.S. Kaverin, I.V. Vilkov, R.I. Korolev, V.N. Sivkov, The identification of cu–o–c bond in cu/mwcnts hybrid nanocomposite by XPS and NEXAFS spectroscopy, Nanomaterials 11 (2021) 2993, https://doi.org/10.3390/NANO11112993/S1.
[50] S. Theodoropoulou, D. Papadimitriou, L. Zoumpoulakis, J. Simitzis, Optical properties of carbon materials formed by pyrolysis of novolac-resin/biomass composites, Diam. Relat. Mater. 13 (2004) 371–375, https://doi.org/10.1016/J.DIAMOND.2003.11.057.
[51] S. Poto, M.A. Llosa Tanco, D.A. Pacheco Tanaka, M.F. Neira d'Angelo, F. Gallucci, Experimental investigation of a packed bed membrane reactor for the direct conversion of CO2 to dimethyl ether, J. CO_2 Util. 72 (2023) 102513, https://doi.org/10.1016/J.JCOU.2023.102513.